Ceramics International 51 (2025) 28935–28953

Contents lists available at ScienceDirect

Ceramics International

journal homepage: www.elsevier.com/locate/ceramint

Advanced hydroxyapatite- DLC bilayer coatings for improved performance of NiTi biomedical alloys

Ali Shanaghi [a,*], Babak Mehrjou [b], Armin Moradjoui Hamedani [a], Ali Reza Souri [a], Abdul Mateen Qasim [b], Paul K. Chu [b,**]

[a] Department of Materials Engineering, Faculty of Engineering, Malayer University, Malayer, Iran
[b] Department of Physics, Department of Materials Science and Engineering, And Department of Biomedical Engineering, City University of Hong Kong, Tat Chee Avenue, Kowloon, Hong Kong

ARTICLE INFO

Handling Editor: Dr P. Vincenzini

Keywords:
Diamond-like carbon
Hydroxyapatite
NiTi alloy
Corrosion resistance
Biocompatibility
Fever conditions

ABSTRACT

Enhancing the performance and biocompatibility of NiTi alloys is crucial for advancing biomedical implant technology. This study aimed to develop and evaluate a novel dual-layer composite coating comprising diamond-like carbon (DLC) and hydroxyapatite (HA) on NiTi alloy, focusing on corrosion resistance, biocompatibility, and antibacterial properties. We applied the coating using plasma immersion ion implantation and deposition (PIII&D) combined with the sol-gel technique, creating a 1.65 μm thick DLC layer and an 800 nm thick HA layer. Corrosion tests were conducted in simulated body fluid (SBF) at 37 °C and 40 °C for 120 h, with electrochemical measurements assessing corrosion potential (Ecorr) and current density (icorr). Biocompatibility was evaluated through nickel ion leaching tests, and antibacterial efficacy was determined using *E. coli*. Results showed remarkable improvements in corrosion resistance compared to single-layer DLC coating, with Ecorr increasing by 36 mV and icorr decreasing by 0.15 μA. cm^{-2} at 37 °C. At 40 °C, Ecorr improved by 298 mV and icorr reduced by 0.17 μA. cm^{-2}. The enhanced protection was attributed to calcium-phosphate precipitation, forming a protective layer on the HA surface. Nickel ion leaching decreased by 47 %, and antibacterial activity against *E. coli* improved by 39 % compared to the uncoated NiTi substrate. These findings suggest that the hydroxyapatite-DLC composite coating offers a promising multifunctional solution for enhancing NiTi biomedical implants, potentially extending implant longevity by up to 30 % and significantly improving patient outcomes.

1. Introduction

NiTi alloys have found applications in various medical fields including maxillofacial surgery, prosthetic implants for living tissues, fracture fixation, lumbar vertebral replacements, and procedures involving the extraction of urinary tract systems or even stenoticarteries and veins [1–5]. These alloys are valued for their exceptional mechanical characteristics like shape memory effect (SME), super-elasticity, and their similarity to human bone properties. Additionally, the existence of a thin native titania layer covering the surface of NiTi further improves its corrosion resistance and biocompatibility behavior [1–6], research findings have confirmed to have low osteogenic (bone-forming) activity [2]. Furthermore, excessive leaching of Ni ions of the alloy into the body ends up in serious health issues such as tissue necrosis, allergic reactions, and even cancer [7].

The surface of materials plays a crucial role in the performance of medical implants, acting as an interface between the material and its environment [8–10]. This importance is amplified for NiTi alloys, as the challenges threatening their biomedical applications extend beyond nickel ion leaching to include corrosion resistance, biocompatibility, and osteogenic activity. Recent studies have explored various coating materials and technologies to improve the properties of NiTi biomaterials, including composite coatings, nanostructures, and advanced surface modification methods. For instance, hydroxyapatite coatings promise improved tissue adhesion, while diamond-like carbon coatings enhance corrosion resistance. Combining these approaches could provide a comprehensive solution for improving the performance of NiTi implants [11–13]. Among the strategies to mitigate Ni release, surface coatings applied by plasma immersion ion implantation and deposition (PIII&D) are particularly attractive. This technique preserves favorable

* Corresponding author.
** Corresponding author.
E-mail addresses: a.shanaghi@malayeru.ac.ir, alishanaghi@gmail.com (A. Shanaghi), paul.chu@cityu.edu.hk (P.K. Chu).

https://doi.org/10.1016/j.ceramint.2025.04.103
Received 10 January 2025; Received in revised form 5 April 2025; Accepted 9 April 2025
Available online 15 April 2025

bulk properties while improving surface characteristics, and its non-line-of-sight nature makes it well-suited for biomedical implants with complex shapes [1,5,6,14–17].

Hydroxyapatite (HA) has similar properties as bones and is used clinically as a coating to improve tissue-implant interactions [6,7]. The orientation of HA crystals' c-axis aligns with the axial direction of collagen bundles where the collagen and apatite minerals have the capability to develop complex composite structures that exhibit favorable mechanical properties [14]. Nevertheless, as a result of the limited adhesion strength between HA and metallic substrates, an interlayer is frequently applied [15]. In this regard, a diamond-like carbon (DLC) film synthesized by PIII&D is a convenient choice due to its chemical inertness, proper biocompatibility, and excellent adhesion strength [16].

Apart from obstacles plaguing implant integration with host tissues, post-operation complications can lead to bacterial infection and symptoms including fever. Upon bacteria attachment, exogenous pyrogens can cause fever and inflammation [17]. When patients suffer from fever, the higher temperature alters the corrosion potentials of metals and more ion leaching may occur [18]. Although the corrosion resistance, toxicity and ion leaching problems associated with NiTi alloys have been studied [19–21], there have been few investigations at elevated temperatures such as fever conditions [22–24]. However, this study explores the innovative application of hydroxyapatite (HA) and diamond-like carbon (DLC) composite coatings on NiTi biomedical alloys, addressing critical challenges in corrosion resistance, biocompatibility, and antibacterial performance under normal and elevated temperature conditions. The novelty of this work lies in the synergistic use of plasma immersion ion implantation and deposition (PIII&D) and the sol-gel process to develop a dual-layer coating system with tailored properties. The DLC layer provides chemical inertness, superior adhesion strength, and enhanced corrosion resistance, while the HA layer promotes osteogenic activity and facilitates calcium-phosphate precipitation for biological integration. For the first time, the corrosion behavior and ion leaching of the coated NiTi alloy are systematically evaluated under simulated fever conditions (40 °C), mimicking post-operative complications. Furthermore, this research aims to bridge the gap between the inherent limitations of NiTi alloys and the stringent demands of modern biomedical applications, offering a comprehensive solution to improve the performance, durability, and safety of implants.

2. Experimental details

The chemicals were chosen based on published data [25–27]. Calcium nitrate tetrahydrate ($Ca(NO_3)_2{\cdot}4H_2O$, 99 %), phosphorus pentoxide (P_2O_5, ≥98.0 %), ethyl acetoacetate (EAcAc) ($C_6H_{10}O_3$, 99 %), and ethanol absolute (CH_3CH_2OH, ≥99.5 %) were acquired from Sigma Aldrich in analytical grade, while ultra refined water was utilized for entire experimental procedures.

2.1. Substrate preparation

The Ni50.8Ti49.2 alloy sheet, containing 50.8 % nickel and 49.2 % titanium by weight, was procured by Sichuan HPM Co, Ltd., China. It exhibits a martensite starting temperature of −12.8 °C and an austenite finishing temperature of 33.4 °C. The alloy sheet was subsequently precision-cut into square specimens measuring 10 × 10 mm^2, having a 2 mm uniform thickness. The specimens were ground using SiC abrasive papers from 400 to 4000 grit and subsequently polished using diamond paste with particle sizes ranging from 100 to 300 nm. The polished specimens were then subjected to a thorough ultrasonic cleaning process for 10 min in acetone (C_3H_6O), ethanol (C_2H_6O), and ultra refined water (H_2O) solvents sequentially.

2.2. Coating preparation

2.2.1. Deposition of DLC coating by PIII&D

Diamond-like carbon (DLC) coatings were deposited on the NiTi alloy specimens using plasma immersion ion implantation and deposition (PIII&D) at the Plasma Laboratory in the City University of Hong Kong. For this process, the NiTi alloy specimens were mounted onto a 100 × 250 mm^2 rectangular stainless-steel substrate. This substrate, bearing the specimens, was then precisely positioned at the center of the vacuum chamber to ensure uniform ion flux and coating deposition. The versatile system show cased a gridless anode layer ion source (ALIS), with the ALIS linked to current-control power units functioning at a frequency of 40.0 kHz and a duty cycle of 80 %. Additional comprehensive details regarding this procedure could be found in published works [25,26].

Then, A 15-min argon glow discharge cleaning process was performed using an argon flow rate of 100 standard cubic centimeters per minute (sccm), a pressure of 1.0 Pa, and a bias voltage of −1.2 kV within the chamber until reaching a base pressure of 2.5 × 10^{-3} Pa. This was followed by ion cleaning with the ALIS at 5.0 × 10^{-2} Pa and an ion current of 0.5 A. After that using the same ALIS featuring a discharge current of 1.0 A, a power output of 700 W, and an Ar to C_2H_2 ratio of 1:5 under a bias voltage of −4.0 [28], caused to deposit of the DLC film. The pressure was maintained between 0.1 and 0.2 Pa using a throttle valve, and the sample stage remained stationary during the 3-h DLC film deposition process.

2.2.2. Fabrication of hydroxyapatite coating by the sol-gel process

The hydroxyapatite layer was deposited by using the sol-gel technique in conjunction with dip coating, were optimized based on our previous findings [26,27,29]. The phosphate solution was prepared at 40 °C by combining 2 mL of ethyl acetoacetate ($C_6H_{10}O_3$) (chelating agent, controls hydrolysis), 50 mL of ethanol (C_2H_6O) (solvent for phosphate precursors), with 3.5 g of phosphorus pentoxide (P_4O_{10}) (phosphorus source), within 10 min. To ensure the stability of the solution, acidic deionized water (hydrolysis agent, pH control), was added in a 1:100 vol ratio, and the mixture was agitated for a day long. A separate nitrate solution was produced by dissolving 19.7 g of calcium nitrate tetrahydrate ($CaH_8N_2O_{10}$) (calcium source), in 50 mL of ultra refined water (H_2O) (solvent), followed by stirring for 40 min at 75 °C. The nitrate solution was then gradually poured into the phosphate solution, and the resulting mixture was agitated for 30 min at pH 2, followed by magnetic stirring at 40 °C for an additional 24 h. The hydroxyapatite coating was deposited onto the substrate using dip coating process at deposition rate of 25 mm/min, with two coating cycles. The coated specimens were subsequently dehydrated and calcined at temperatures of 80, 120, and 500 °C for duration of 30, 30, and 120 min, respectively, with a heating rate of 1 °C/min. The NiTi alloy with a single DLC coating and the dual HA-DLC structure was designated as 'DLC-NiTi' and 'HA-DLC-NiTi', respectively.

2.3. Characterization

2.3.1. Structure

Various analytical methods were employed to analyze the phase, structure, chemical composition, and surface morphology of the coatings in detail. Grazing-incidence X-ray diffraction (GIXRD) analysis was carried out through a Philips PW-1730 X-ray diffractometer with Cu Kα radiation (λ = 0.154056 nm). The grazing incidence angles used were 1°, 3°, and 7°, and diffraction patterns were recorded in the 2θ range of 10°–80°, with a step size of 0.02°. X-ray photoelectron spectroscopy (XPS) measurement was performed on a PHI 5802 instrument by ULVAC-PHI Inc., Japan, employing monochromatic Al Kα radiation. Field-emission scanning electron microscopy (FE-SEM) images were obtained using a JSM-7001F microscope (JEOL Ltd., Tokyo, Japan), while atomic force microscopy (AFM) analysis was conducted on a

Nanoscope V Multi Mode System from Veeco. The crystallite size and lattice strain were calculated using High Scoreplus software and the Scherrer formula [30], while the film thickness was measured by the XPS depth profile.

2.3.2. Corrosion properties

The corrosion test was conducted in a simulated body fluid (SBF) which comprised 7.996 g of sodium chloride (NaCl), 0.35 g of sodium bicarbonate ($NaHCO_3$), 0.224 g of Potassium chloride (KCl), 0.228 g of dipotassium hydrogen phosphate trihydrate ($K_2HPO_4.3H_2O$), 0.305 g of magnesium dichloride hexahydrate ($MgCl_2.6H_2O$), 40 mL of 1 Molar of hydrogen chloride (HCl), 0.278 g of calcium chloride ($CaCl_2$), 0.071 g of Sodium sulfate (Na_2SO_4), and 6.057 g of tris(hydroxymethyl)aminomethane ($((CH_2OH)_3CNH_2)$) at 37 ± 0.5 °C and pH of 7.40 ± 0.01 in accordance with the standard procedure established by Kokubo [28]. The chemical reagents supplied by Merck company were gently added to 1 L of deionized water without undergoing additional purification processes.

Electrochemical impedance spectroscopy (EIS) and potentiodynamic polarization tests have been performed by utilizing an electrochemical workstation (Zennium, Zahner, Germany). The evaluation of the corrosion performance was conducted using a cell configuration where the sample served as the working electrode, a standard calomel electrode (SCE) was employed as the reference electrode, and the platinum mesh was used as the auxiliary electrode. The corrosion experimentshave beendone in 250 ml of simulated body fluid (SBF). The working electrode was created by attaching a copper wire to the rear of the specimen using silver adhesive, while the rear and sides were coated with silicon glue to expose an area of approximately 1 cm^2. The open circuit potential (OCP) was measured at 37 °C for the initial 35 min of immersion. EIS measurements were conducted over a frequency range of 10^{-1} to 10^5 Hz with an amplitude of 10 mV and a frequency of 20 MHz in a sweeping mode. Potentiodynamic polarization scans were carried out from −250 mV to +1000 mV as opposed to the open circuit potential (OCP) at a scan rate of 1 mV s^{-1}. Parameters of corrosion testing such as corrosion current (icorr) and potential (Ecorr) were measured utilizing Tafel extrapolation, while the passivation current (ipassive) was obtained from the vertical part of the anodic branch. To study the corrosion mechanism, impedance tests were conducted after immersion periods of 1, 24, 48, 72, 96, and 120 h in SBF, followed by a potentiodynamic polarization test after 120 h of immersion. Corrosion resistance was evaluated through impedance tests at 37 °C (normal condition) and 40 °C (elevated temperature) after 96 and 120 h of immersion in SBF, with polarization tests conducted after 120 h. The corroded surfaces were analyzed using the GIXRD technique at an incident angle of 1°. The quantity of nickel ions released into the simulated body fluid (SBF) solution after a 120-h exposure at a temperature of 37 °C, following polarization and antibacterial testing, was quantified using inductively coupled plasma mass spectrometry (ICP-MS) with a PerkinElmer Optima 2100 DV instrument.

2.3.3. Nano-mechanical properties

The nano-mechanical characteristics, such as Young's modulus (E) and hardness values, were assessed by nano-hardness testing conducted with the HysitronTriboScope device. Nano-indenters with a spherical diamond tip (1 μm radius) produced by D.R. U.D. Hangen at SURFACE, Huckelhoven, were employed with the NanoScope III atomic force microscopy (AFM). These tests were conducted utilizing the load control method [31], where the load applied to the indenter was incrementally raised until reaching a specific maximum load, after which it was consistently decreased to zero level. The recorded data includes the amount of load and the displacement of the diamond tip, which were then used to calculate the hardness and elastic modulus [32]. These calculations have been performed using the Oliver-Pharr method, which involves analyzing the loading and unloading curves [33]. Every experiment was redone five times consecutively to ensure statistical reliability. The adhesion strength was assessed by employing a micro-scratch tester equipped with a diamond tip measuring 0.1 mm. The adhesion strength evaluation was performed by employing a micro-scratch tester equipped with a diamond tip having a radius of 0.1 mm. The minimum load necessary for the coatings to start delaminating from the NiTi alloy substrate, along with a sudden rise in the depth of the indenter, was defined as the critical load (L).

2.3.4. Bacteria and cell studies

The antibacterial properties of the samples were assessed following a standard protocol outlined in literature [34]. Initially, Escherichia coli (*E. coli*) (ATCC 25922) bacteria were cultured in Lysogeny Broth (LB) medium at 37 °C while stirring at 220 rpm for 12 h during the night. The bacterial density was adjusted to an optical density of 0.1 (OD600 = 0.1) by introducing a fresh medium and further incubated for 3 h. Subsequently, the bacterial concentration was adjusted to 2-3 × 10^5 CFU/mL (colony-forming units), and 100 μL of this solution was inoculated onto the samples. Prior to bacterial inoculation, three samples from each group were treated with 75 % ethanol for 20 min, dried in a bio-safety cabinet, and exposed to UV light on each side for approximately 30 min. After 6 and 24 h, the specimens have been analyzed by utilizing the scanning electron microscopy (SEM) technique following the removal of the culture medium, washing with PBS to eliminate unattached bacteria, and fixation with 2.5 % glutaraldehyde ($C_5H_8O_2$) solution overnight. Specimens underwent dehydration through a sequence of ethanol solutions followed by air-drying at room temperature. In the colony-forming unit (CFU/mL) counting experiments, the bacterial suspension from the 24-h specimen was serially diluted, plated on agar, and incubated at 37 °C overnight.

To conduct the cell study, The MC3T3-E1 osteoblast cell line, which was acquired from the Cell Bank of the Chinese Academy of Sciences, have been employed. The cells have been cultured in a humidified incubator containing 95 % air and 5 % CO_2 gas. Following detachment with Trypsin, a cell suspension containing approximately 20,000 cells/mL was seeded onto the samples in a 24-well plate, supplemented with Dulbecco's Modified Eagle's Medium (DMEM). The culture medium was refreshed every 48 h, and each test was conducted 3 times to ensure reliability and accuracy. Cell proliferation was quantitatively determined by using a MTT (3-(4,5-dimethylthiazol-2-yl)-2,5-diphenyltetrazolium bromide) assay. After cells growing for 1, 4, and 7 days, a 5 mg/mL MTT solution was added to react with the cells, followed by dissolution of formazan crystals with dimethyl sulfoxide (DMSO). The optical density have evaluated at 570 nm using a multimode reader (BioTek), with pure DMSO serving as the control.

2.4. Statistical analysis

The corrosion and biological tests were carried out five times, and the results were reported as mean ± SD (standard deviation). A one-way ANOVA was conducted using Microsoft Excel to assess statistical significance, with results considered significant at $P < 0.05$.

3. Results and discussion

3.1. Phase and structural characteristics of DLC-NiTi and HA-DLC-NiTi

The crystal structure of the DLC and HA-DLC coatings are identified from the GIXRD patterns (Fig. 1a–b) by indexing based on the cards of $Ca_{10}(PO_4)_6(OH)_2$ (PDF 01-072-1243),$Ca_{10}(PO_4)_6CO_3$ (PDF 00-035-0180), diamond (PDF 01-079-1473), carbon (PDF 00-026-1082), and titanium oxide (PDF 01-086-2352) of the International Center for Diffraction Data (ICDD). According to the GIXRD pattern of the DLC coating (Fig. 1a, acquired at 1°, two phases of rhombohedral crystalline diamonds well as hexagonal crystalline carbon structure are detected to confirm the formation of the DLC layer on the NiTi substrate. The crystallite size of the diamond is about 9 nm with 1.125 % lattice strain.

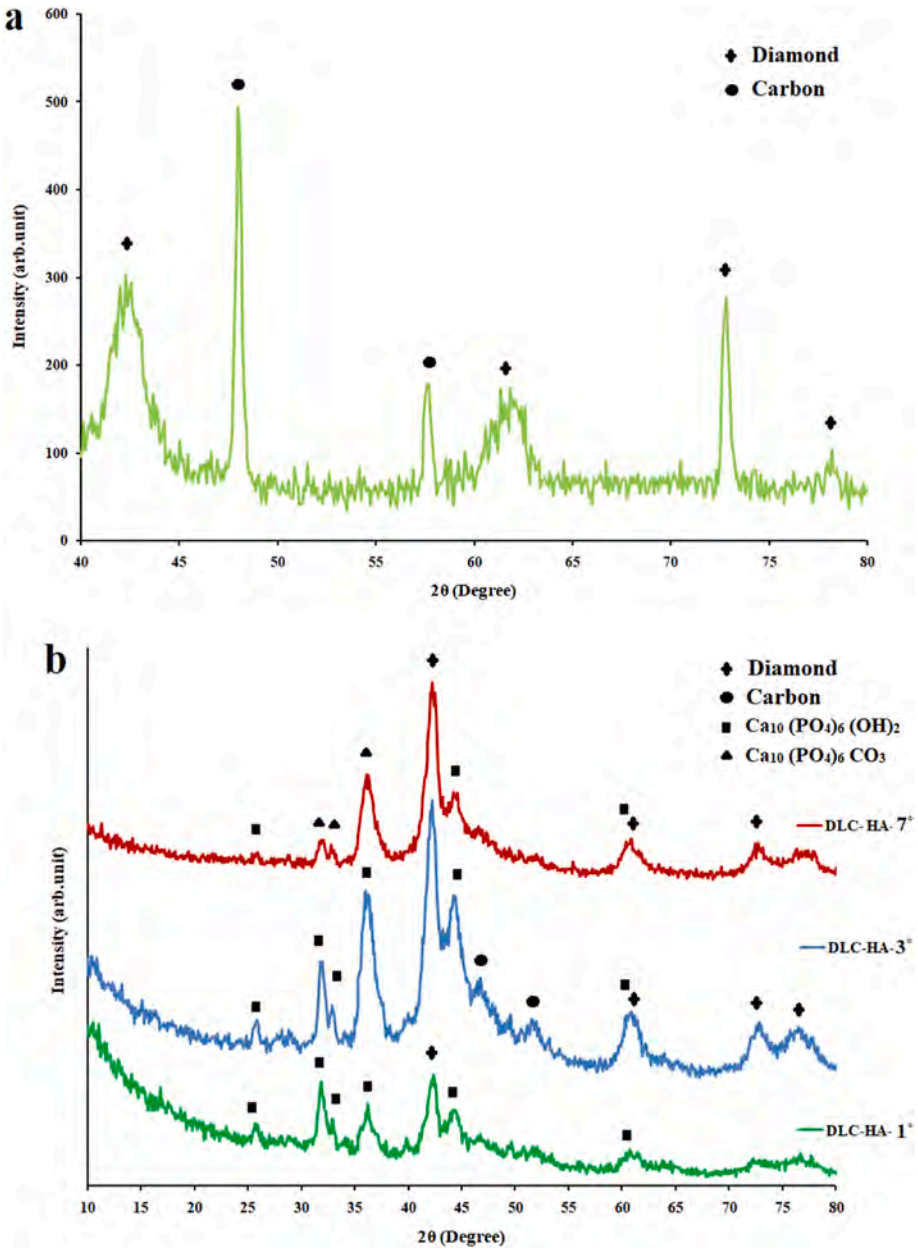

Fig. 1. GIXRD patterns: (a) DLC sample at 1° incident angle and (b) DLC-HA sample at three different incident angles of 1°, 3°, and 7°.

Similarly, the GIXRD pattern of the HA-DLC film (Fig. 1b) shows characteristic peaks of HA as well as ones related to DLC. The crystallite size of HA is about 8 nm with 1.359 % lattice strain. By increasing the incident angle to 7 °, the DLC peaks become stronger because of the porous microstructure of HA. The corresponding peak of calcium phosphate carbonate formed as a transition layer from HA to DLC after the heat treatment at 500 °C emerges at 7° [34,35]. , which may be due to the reaction between the graphitic component in the DLC coating with calcium and phosphate ions during the heat treatment at 500 °C, which confirmed by the FE-SEM images (Fig. 2) show a porous DLC coating.

These results also reveal the physically and chemically adhered interface between the sol-gel hydroxyapatite coating and DLC coating. The DLC-HA sample has a particle size of about 35 nm, and a porous and flake-like structure is observed from the hydroxyapatite coating (Fig. 2). The morphology and particle size of the DLC coating play an important role in nucleation and adhesion properties of HA deposited by the sol-gel on DLC.

The AFM images (Fig. 3) and the surface roughness (Table 1) illustrate that the DLC-HA has reduced surface roughness (Sa) of 91 nm compared to 306 nm of the DLC coating. It is due to filling of defects and pores in the DLC coating by the hydroxyapatite coating. Due to low heat treatment temperature of hydroxyapatite layer, The adhesion mechanism of the hydroxyapatite coating is mainly physical. According to Fig. 3a, the needle-shape morphology of the DLC coating increases adhesion of the hydroxyapatite coating.

The survey XPS spectrum of DLC-HA samples (Fig. 4a) reveal peak of Ca3p, Ca3s, P2p, P2s, C1s, Ca2p, and O1s at 25.6, 44.8, 132.8, 189.6, 284.7, 350.4, and 529.6 eV, respectively [36,37]. Comparing the photoelectron signals of Ca, P and O of the hydroxyapatite coating in DLC-HA [35], the Ca2p peak (Fig. 4b) consists of two peaks with binding energies of 347.8 eV for Ca2p3/2 and 351.4 eV for Ca2p1/2 along with the P2p peak at 133 eV (Fig. 4c) confirming the formation of the hydroxyapatite coating in the DLC-HA sample [38]. According to the literature [39–42], the carbon bonds (Fig. 4d) can be determined from C1s at 282.6 eV, Csp2 at 284.5 eV, and Csp3 at 285.2 eV and the percentages are 31 %, 23 %, and 15 %, respectively. The peak at 288.1 eV

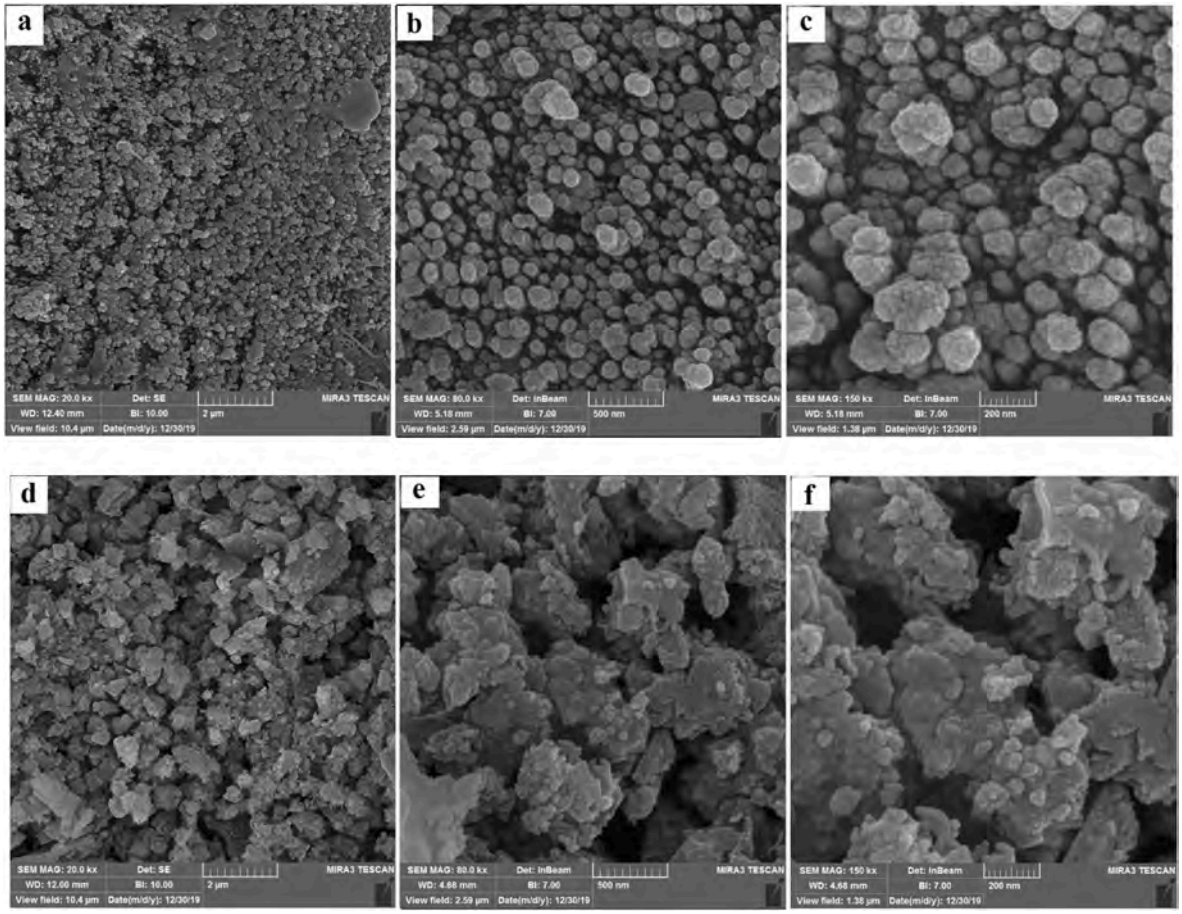

Fig. 2. FE-SEM images: (a–c) DLC and (d–f) DLC-HA at magnifications of 20, 80, and 150 kX.

can be assigned to carbons as a part of the carbonyl (C= O) in the hydroxyapatite coating.

To clarify the formation and composition of the multilayer coating, XPS depth profiling was performed (Fig. 4e), revealing a total thickness of 2.6 μm with distinct regions. The surface layer (10–20 nm) shows high concentrations of carbon and oxygen, primarily attributed to atmospheric contamination and surface oxides, which do not affect the coating's performance [36–41]. From 20 to 800 nm, significant levels of calcium, phosphorus, and oxygen indicate the formation of a uniform hydroxyapatite (HA) layer, serving as the bioactive surface. The coating can be divided into three main parts: a top hydroxyapatite layer approximately 800 nm thick, a 600 nm transitional layer of calcium phosphate carbonate compounds penetrating the defects of the needle-structured DLC coating, and a 1.65 μm DLC layer with a 110 nm diffused interface. The gradual decrease in Ca and P distribution between 800 and 1600 nm confirms the presence of a calcium phosphate diffusion layer within the DLC structure. High carbon and oxygen concentrations from 1600 to 2600 nm depth indicate the DLC base layer, and a significant increase in titanium concentration beyond 2600 nm marks the transition to the titanium substrate, ensuring strong adhesion between the coating and the substrate. The results confirm the different compounds detected by GIXRD at 1°, 3° and 7° incident angle.

3.2. Corrosion behavior

The E-t curves of the NiTi alloy, DLC, and DLC-HA samples in SBF (Fig. 5) reveal initial potentials of −167.3, 76.1 and 139.8 mV, respectively. With increasing immersion time, the potential of the NiTi alloy and DLC-HA are almost constant with only slightly shift towards negative values due to enhanced corrosion reactions, especially DLC-HA. Soluble ions such as Cl^- penetrate the pores and defects in the hydroxyapatite layer and DLC layer into the NiTi alloy and increased substrate dissolution decrease the potential associated with oscillation. As a result of porous structure of hydroxyapatite layer can be considering two types anodic and cathodic reactions, the anodic reaction formula, Eq. (1), Eq. (2) or Eq. (3), and cathodic reaction formula, Eq. (4) for localized corroded part, which this phenomenon is related to the formation of corrosion products at the anodic and localized areas (porosity of the hydroxyapatite coating), and the anodic reaction formula, Eq,(5), and cathodic reaction formula, Eq. (6) for other parts of surface [6,7]:

$$Ti^{4+} + 4Cl^- \rightarrow TiCl_4 \quad (l)$$

$$TiCl_4(l) + 2H_2O \rightarrow TiO_2(s) + 4H^+ + 4Cl^- \quad (2)$$

$$Ti + 2H_2O \rightarrow TiO_2 + 4H^+ + 4e^- \quad (3)$$

$$O_2\,(g) + 4H^+(aq) + 4e^- \rightarrow 2H_2O(l) \quad (4)$$

$$Ni \rightarrow Ni^{+2} + 2e^- \quad (5)$$

$$O_2 + H_2O + 4e^- \rightarrow 4\,OH^- \quad (6)$$

In general, ceramic coating acts as a barrier against movement of ions and electrons resulting in a more positive potential compared to the bare NiTi alloy [6,7]. A more negative potential of DLC-HA than DLC can be related to release of hydrogen from the former by the cathodic reaction with water or limit cathodic reaction by oxygen access and hence dependent on mass transport, Eq. (4). The hydroxide ion comes from SBF solution and cathodic reaction, Eq. (6), helps to deposit calcium phosphorus compounds at the defects of the hydroxyapatite coating from SBF [43].

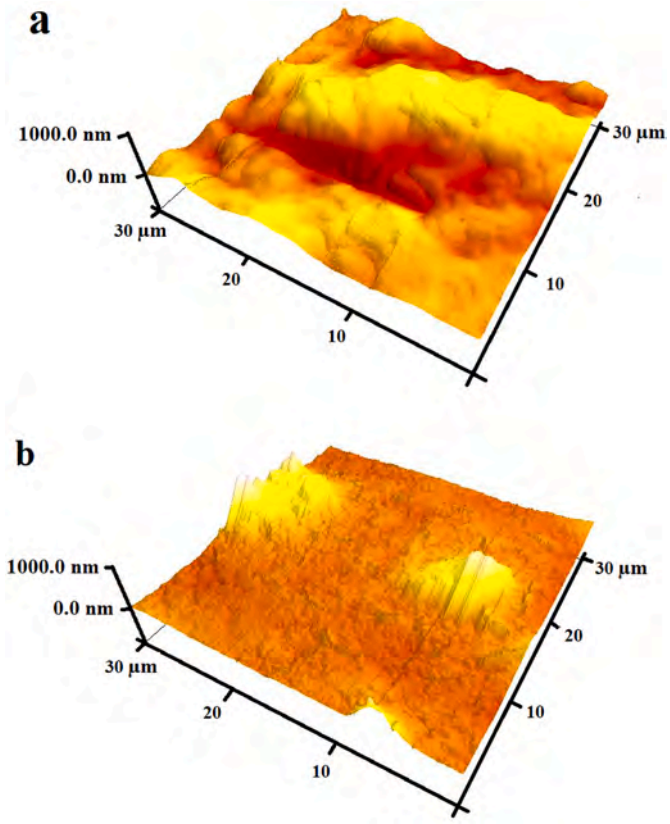

Fig. 3. AFM images: (a) DLC and (b) DLC-HA samples with a z-scale of 1000 nm.

Table 1
Surface roughness valuesof the NiTi alloy, DLC and DLC-HA samplesderived by AFM.

Sample	NiTi alloy	DLC	DLC-HA
Surface roughness (Sa) (nm)	118 ± 35	306 ± 18	91 ± 11

The Nyquist, Bode, and Bode-phase plots of samples after immersion for 1, 24, 48, 72, 96, and 120 h in SBF are presented in Figs. 6 and 7. DLC-HA has the highest impedance modulus at immersion for 1 h along with a sharp decrease at 24 h and significant increase at 72 h immersion compared to the other samples. Initially, the coating provides a high level of protection at 1 h, indicated by a high impedance modulus. However, after 24 h, the impedance decreases sharply, likely due to partial degradation or penetration of the electrolyte through defects in the coating. By 72 h, the impedance increases significantly, suggesting the formation of a new protective layer through the deposition of calcium phosphate compounds, such as hydroxyapatite. The results indicate chemical and electrochemical interactions such as deposition of corrosion products and calcium phosphate on the surface of DLC-HA to make it more biocompatible [6,7,43].

Penetration of corrosive ions and water into the surface of NiTi alloy at high frequencies and reduction of impedance modulus at low frequencies decrease the corrosion resistance of the NiTi alloy sample as the immersion time is increased to 24 h. The DLC coating increases the corrosion resistance up to 48 h by sedimenting corrosion products from SBF solution on the corroded surface as confirmed by Nyquist, Bode and Bode-phase plots (Figs. 6 and 7a-b). However, the more stable of bode-phase plot at high frequencies reflects the small interactions between SBF and DLC and indicates low biocompatibility of DLC. Although, the porous structure of the hydroxyapatite of DLC-HA and localized corrosion state decrease the corrosion resistance during immersion for 24 h, probably sedimentation of corrosion products and calcium and phosphate ions from SBF on the defects and pores of the hydroxyapatite coating increases the corrosion resistance significantly. It is in agreement with the phase angles at high frequencies (Bode-phase plot) that provide evidence of enhanced corrosion resistance and a capacitive behavior for DLC-HA.

Actually, electrochemical analysis revealed a complex interaction of corrosion and surface modification. Although hydroxyapatite (HA) typically promotes apatite formation in simulated body fluid (SBF) [6,7,35,36], which can improve corrosion resistance, an opposing trend was observed for the DLC- HA coating. This seemingly contradictory behavior is attributed to electrolyte penetration through the porous HA layer, leading to accelerated corrosion of the underlying layers. Initial apatite formation is insufficient to counteract this corrosion. Over time, corrosion products and calcium phosphate deposit within the pores, partially blocking the electrolyte path and increasing impedance. However, the initial damage compromises the coating's protective ability, indicating that the HA layer's porosity becomes detrimental before apatite formation can dominate.

The mechanism and corrosion behavior are investigated with an electrical equivalent circuit model constructed to simulate the electrochemical cell [44,45]. The electrical equivalent circuit models of the NiTi alloy, DLC, and DLC-HA samples are presented in Fig. 8 and the results are summarized in Tables 2 and 3. R_s, R_{HA}, R_{DLC}, R_{pro}, and R_{ct} are related to the SBF solution resistance, hydroxyapatite coating, DLC layer, corrosion products and charge transfer resistance. CPE_{HA}, CPE_{DLC}, CPE_{pro}, and CPE_{dl} are related to the hydroxyapatite coating capacitance, DLC coating capacitance, corrosion products capacitance, and charge transfer capacitance, and d and n is the thickness of double layer, which calculated by result of Hirschorn and et al. [44], and a measure of the surface roughness and uniformity, respectively. To validate the accuracy of the electrical equivalent circuit models, the fitted curves of DLC and DLC-HA samples after immersion for 72 h are shown in Fig. 9a–b, respectively, and the Chi-square results in Tables 2 and 3 indicate a good fit.

Tables 2 and 3 show enhanced corrosion resistance of the NiTi alloy with DLC. With immersion time over 24 h, the coating resistance decreases and R_{ct} is observed from the electrical equivalent circuit. The double layer capacitance is a measure of the permeability of the solution and corrosive ions and so the rising CPE_{dl} without increasing the layer thickness for immersion time up to 72 h indicates incremental degradation at the interface between the DLC layer and NiTi alloy, so as to was confirmed by increasing thickness of double layer to 20 nm at 120 h immersion time. This is accompanied by formation of corrosion products (maybe titanium oxide) in the defects and degraded area as shown by CPE_{pro} and R_{pro} in the electrical equivalent circuit at 96 h. Penetration of corrosive ions for 120 h causes the observed double layer. However, in DLC-HA, the porous structure of hydroxyapatite in the top layer increases localized corrosion resulting in significant decrease in the corrosion resistance compared to the DLC coating after 24 h, as shown by CPE_{dl} and R_{ct} of the double layer in the electrical equivalent circuit. A larger CPE_{dl} coupled with small R_{ct} indicates degradation of the interface between the DLC coating and NiTi alloy after 24 h. Absorption and sedimentation of calcium and phosphate ions and corrosion products (titanium oxide) from the hydroxyapatite layer and substrate corrosion reaction of NiTi alloy as a substrate are observed after 48 and 72 h and the corrosion behavior of DLC-HA resembles that of DLC [6,7,44–47]. Decreasing R_{pro} and increasing ion and electron transfer and anodic reactions lead to substitute R_{ct} instead of R_{pro} at 96 and 120 h. These results are in agreement with Ref. [47] which reports a low Ni concentration on the corroded surface suggesting that pitting corrosion results in nickel release from the bulk to the NaCl solution. Meanwhile, the remaining Ti reacts with dissolved oxygen in the solution form titanium oxide in the corroded area, which demonstrated by decreased thickness of double layer from 16 nm for 120 h compare to 152 nm for 96h.

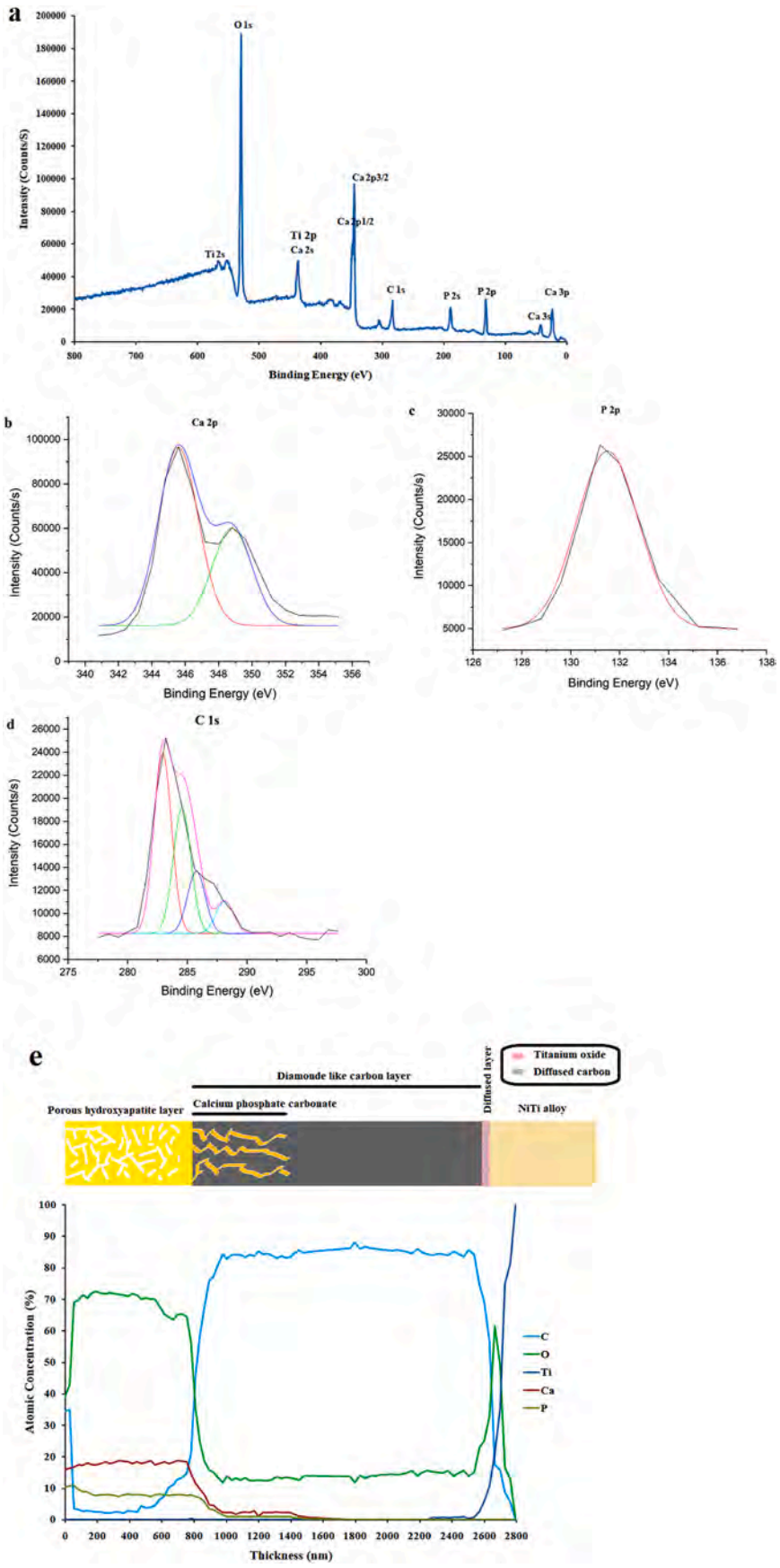

Fig. 4. (a) Survey XPS spectra of DLC-HA; High-resolution spectra: (b) C1s, (c) Ca2p, (d) P 2p; (e) XPS depth profiles of DLC-HA.

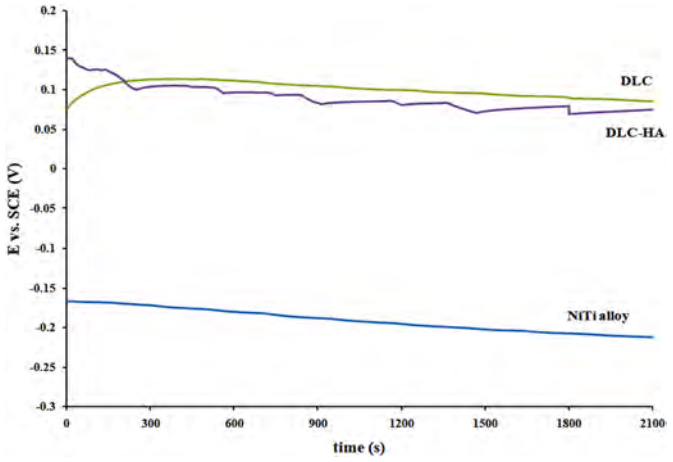

Fig. 5. E-t plots of NiTi alloy, DLC and DLC-HA samplesafter immersion for 2100 s in SBF.

The hydroxyapatite layer as suitable sites for adsorption and sedimentation of calcium and phosphate ions from SBF and corrosion products from the substrate (titanium oxide) can be reduce defects in DLC-HA to improve the corrosion resistance. The decreasing trend of n_{coat} of DLC-HA from 1 h to 24 h confirms localized corrosion due to the porous structure of the hydroxyapatite layer and n_{coat} remains almost constant up to 120 h corroborating deposition of calcium and phosphate ions and corrosion products. It should be noted that a uniform corrosion state is dominant at the DLC layer compared to DLC-HA.

3.2.1. *Effects of fever on the corrosion behavior*

Since the corrosion reactions depend on thermodynamics and kinetics and movement and penetration of ions, it is important to investigate the effects of elevated temperature for postoperative fever and infection. The Nyquist, Bode, and Bode-phase plots of DLC and DLC-HA samples at immersion time of 96 h and 120 h at 40 °C (Fig. 10) indicate that the corrosion resistance of the DLC sample decreases as the temperature is raised from 37 °C to 40 °C during 96-h immersion but the mechanism of corrosion behavior is the same according to the Bode and Bode-phase plots (Fig. 10b–c)). This is related to the increases movement of ions in SBF and easier release of Ni ions. Actually, this phenomenon in the human body can be exacerbated by impairment of enzymes and proteins as well as growth of microorganisms around the coating [48,49]. Fig. 10d–f, indicate that the corrosion resistance of DLC-HA at 96 h–120 h at 37 °C and 40 °C is the same. Nonetheless, a higher temperature increases movement of calcium and phosphate ions leading to more effective formation of calcium phosphate and improved biocompatibility. Since the porous structure of hydroxyapatite allows the flow of extra cellular fluid to enhance the osteo-conductivity, adhesion is improved [44,50].

Because the corrosion behavior of the DLC and DLC-H coatings is stable, the equivalent circuit does not change appreciably. Table 4 indicates increased coating resistance of DLC-HA as the temperature is increased from 37 °C to 40 °C compare to the DLC coating which shows decreased coating resistance. In fact, it reflects absorption of calcium and phosphate ions from SBF and eventual increased corrosion resistance of DLC-HA. Finally, reduction of corrosion resistance of DLC increases Ni^{+2} release and reduced biocompatibility compared to DLC-HA.

Fig. 11 presents the polarization plots of the NiTi alloy after 24 h and DLC and DLC-HA after 120 h in SBF at 37 °C and 40 °C and the results are summarized in Table 5. The corrosion current density (i_{corr}) is derived by extrapolating the cathodic branch of the polarization curves to the OCP as the anodic curves do not possess distinct Tafel regions. The corrosion rate (v_{corr}) is calculated by Eq. (5) [51,52]:

$$Corrosion\ Rate\ \left(mm.y^{-1}\right) = \frac{i_{corr}.K.EW}{d.A}, \tag{5}$$

where the constant, K = 0.00327 defines the corrosion rate (mmy^{-1}), i_{corr} is the corrosion current density in μA cm^{-2}, ρ is the density of the corroding material, NiTi alloy, (6.45 g m^{-3}), and *EW* is the equivalent weight (53.37 g). Deposition of DLC and DLC-HA shifts E_{corr} to more positive values of −225 mV and −189 mV and reduces the corrosion current densities to 0.19 and 0.04 μA. cm^{-2} compared to the NiTi alloy. The reduced cathodic and anodic branch slope, especially the anodic branch, indicates improved corrosion resistance and more effective anodic reactions compared to the cathode reactions along with deposition of uniform and compacted calcium phosphate as corrosion products (hydroxyapatite confirm by GIXRD in Fig. 12) in SBF at 37 °C. This produces passivation layers on DLC and DLC-HA after immersing for 120 h. Although, the distinct peak in anodic branch at 0.15 V for the DLC sample at both 37 and 40 °C, and changing $i_{passive}$ of DLC-HA at 37 °C, confirm more stability of passivation layer for DLC-HA at 40 °C, which caused to diminish Ni ion release about 92.25 and 95.88 % compare to NiTi alloy, at both 37 and 40 °C, respectively.

A higher SBF temperature of 40 °C gives rise to increased permeability and movement of calcium and phosphate ions as well as changes in the function of enzymes and proteins in the human body [48,49], consequently decreasing the corrosion resistance of the DLC coating, increasing the corrosion current density to 0.23 μA. cm^{-2}, and shifting the corrosion potential to a more negative value of −295 mV. In contrary, the higher SFB temperature improves the corrosion resistance of DLC-HA as manifested by shifted potential to more positive from −295 ± 1 to 3 ± 1 mV and corrosion current density from 0.23 ± 0.03 to 0.06 ± 0.02 μA. cm^{-2}, besides the creation of a more stable passive layer at 40 °C. The DLC-HA double layer has higher corrosion resistance and is more durable than a single-layer DLC coating as confirmed by GIXRD conducted after the corrosion test (Fig. 12). In fact fever increases the mobility of calcium and phosphate ions as well as penetration of corrosive ions such as Cl^- eventually forming a single-phase hydroxyapatite layer on the surface of DLC-HA.

Actually, the observed shift in corrosion behavior at 40 °C stems from competing effects on both the DLC and HA-DLC coatings. For DLC, the increase in ionic mobility accelerates the penetration of corrosive ions (e.g., Cl^-) through inherent defects in the film, enhancing the dissolution of the NiTi substrate and leading to a decrease in corrosion resistance. The permeability of the DLC is increased in high temperature, and as a result, the barrier protection is decreased. This is also partially caused by thermal expansion that makes it more corrosion susceptible [35,39,51,52]. For HA-DLC, the increased mobility of calcium and phosphate ions initially enhances the formation of the calcium phosphate-rich passive layer, leading to improved corrosion resistance at 40 °C. The increased temp provides to not have limited protection of diffusion. However, this enhanced deposition is also influenced by the thermodynamics of the reactions. At higher temperatures, the solubility of calcium and phosphate increases, potentially affecting the morphology and composition of the deposited layer [26,27,29,36]. Also, the corrosion reaction increased as well, as shown in Fig. 7. However, these competing kinetic and thermodynamic factors necessitate a more comprehensive analysis of the surface composition and structure following SBF immersion at both 37 °C and 40 °C.

3.3. *Nano-mechanical properties*

When a force is applied to a material, its mechanical response is governed by its elastic properties, including Young's modulus and Poisson's ratio (ν). Poisson's ratio, a dimensionless parameter, quantifies a material's propensity to deform in directions perpendicular to the applied load under uniaxial stress, representing the ratio of transverse strain to axial strain [31,53]. For the interpretation of nanoindentation

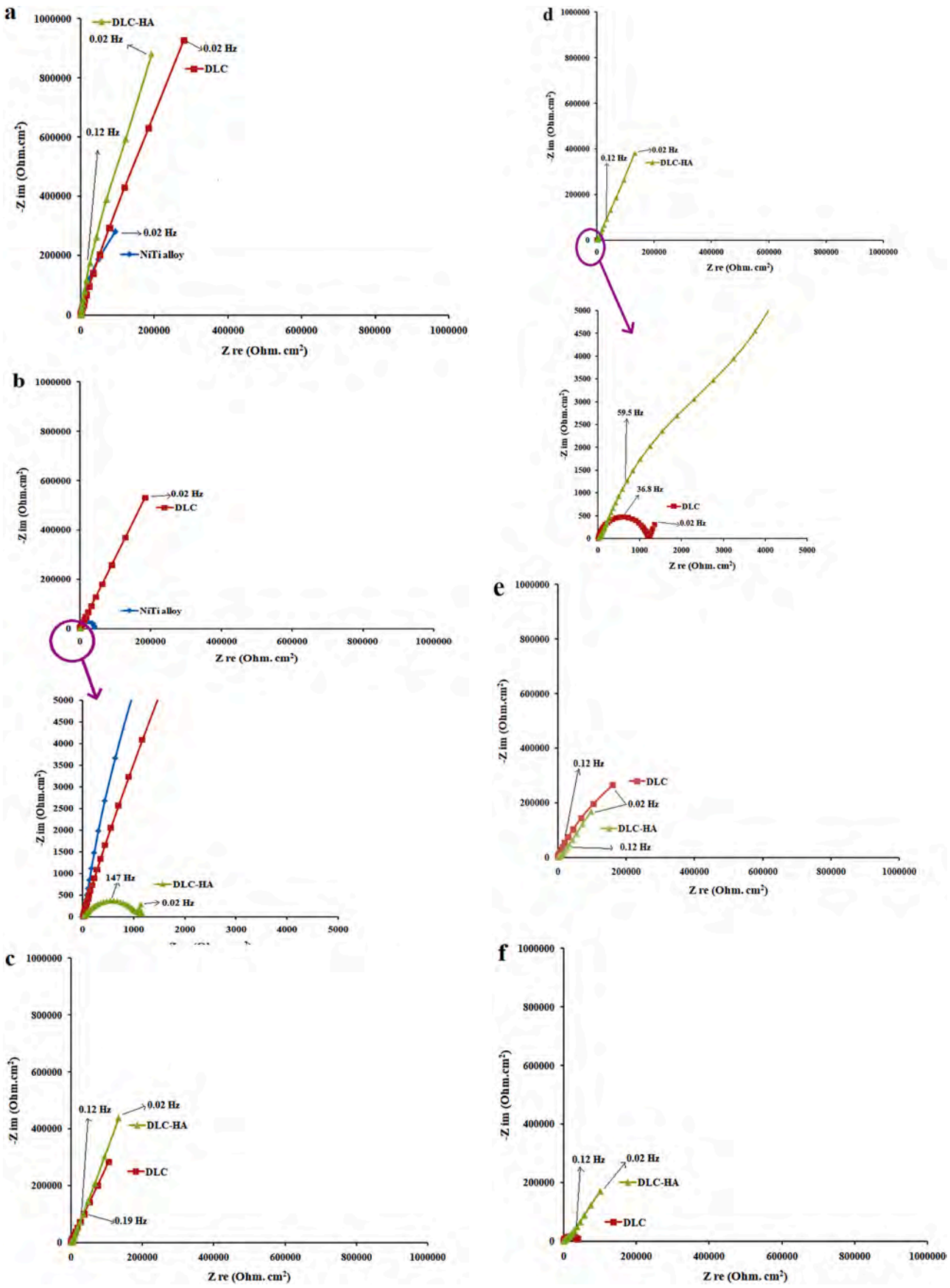

Fig. 6. Nyquist plots ofthe NiTi alloy, DLC and DLC-HA samples: (a) 1 h, (b) 24 h, (c) 48 h, (d) 72 h, (e) 96 h, and (e) 120 h immersion in SBF solution.

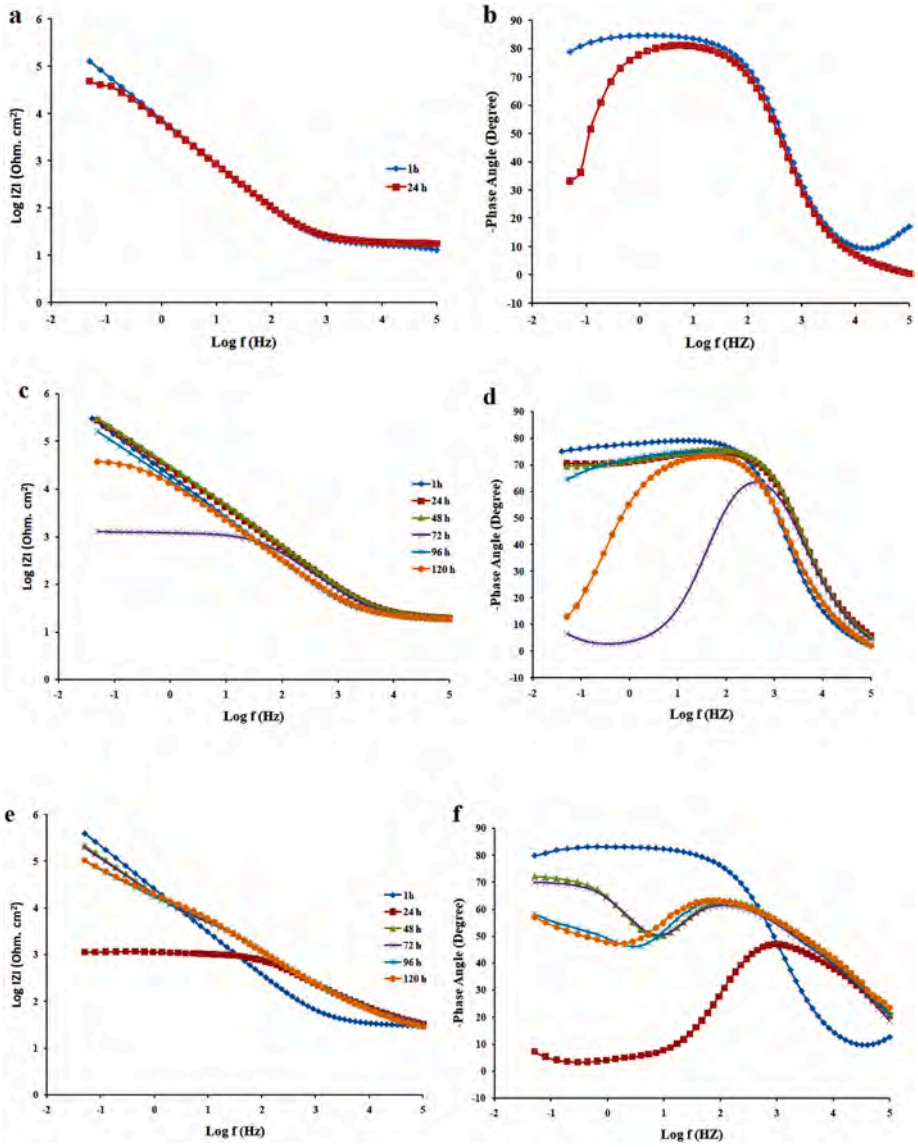

Fig. 7. Bode and Bode- Phase plots:(a–b) NiTi alloy at 1 and 24 h, (c–d) DLC sample, and (e–f) DLC-HA at different immersion time of 1, 24, 48, 72, 96 and, 120 h in SBF solution.

data, precise evaluation or appropriate consideration of Poisson's ratio is of paramount importance, as it affects the contact area and the computed hardness and modulus [33]. In this investigation, established literature values were employed: Poisson's ratio was assumed to be 0.32 for the NiTi substrate [54], 0.25 for the DLC coating [55], and 0.30 for the HA coating [56]. Although not experimentally determined in this study, these values offer a sound basis for analyzing the nanoindentation results and elucidating the materials' behavior under localized deformation. The nano-mechanical properties such as hardness and wear behavior are evaluated by nano-indentation and nano-scratch test, respectively, and the results are summarized in Table 6. The one-tenth rule of coating thickness is adopted to control the depth of indentation and eliminate effects of the substrate [22,57,58]. The DLC coating on NiTi shows increased hardness from 5.36 GPa to 13.42 GPa, but the DLC-HA double layer shows reduced hardness to 2.1 GPa (Fig. 13). The decrease in hardness is due to the porous, sheet-like, and more fragile hydroxyapatite coating [4]. Sidanea et al. [3] have reported that the hardness of hydroxyapatite coatings is in the range of 0.4–0.6 GPa. Owing to the one-tenth rule and the middle DLC coating, the hardness of the DLC-HA coating increases by 2.1 GPa. In the TiO_2-HA double layer, the TiO_2 middle layer plays an important role in the mechanical properties of hydroxyapatite coating [22]. A 2.38 N critical load of DLC-HA and hertzian pressure and shear stress of 2325.6 and 742.6 MPa at a maximum depth of about 4 μm indicate good adhesion of the hydroxyapatite coating to DLC consistent with the literature [21,22,59] boding well for tissue engineering. The rate of displacement due to constant loading at the top of the nano-indentation plot indicates increased elongation capability of DLC-HA compared to DLC. The creep behavior of DLC-HA is suitable for biomedical application and similar to that of the NiTi alloy substrate [57,58].

Fig. 14 illustrates that the scratches on the DLC layer are sharper with less accumulation around the tracks compared to other samples and abrasive wear is dominant. According to Fig. 14a and b, the adhesion wear mechanism is dominant for NiTi. However, the roughness of the path of the indenter and accumulation on DLC-HA (Fig. 14e–f) indicate that the adhesion mechanism dominates along with plastic deformation, which improves the mechanical behavior of DLC-HA compared to DLC [21,22,42,57–59]. The friction vs. time plots of NiTi, DLC, and DLC-HA from the scratch test (Fig. 15) show average friction coefficients of 0.447 ± 0.032, 0.054 ± 0.017 and 0.304 ± 0.027 for the NiTi alloy, DLC and DLC-HA samples.

In general, DLC coatings have small friction coefficients due to the

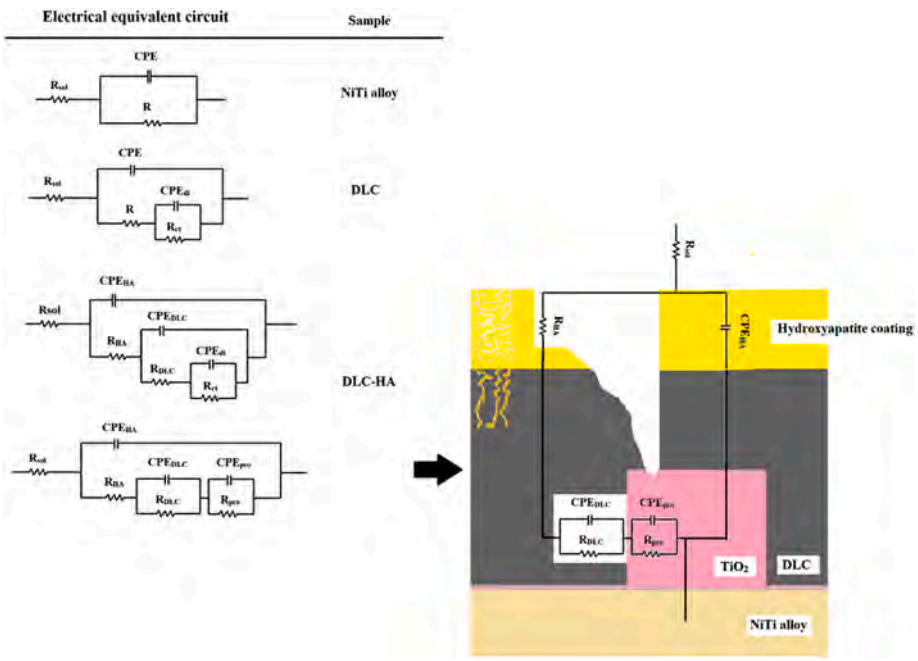

Fig. 8. Electrical equivalent circuits ofthe NiTi alloy, DLC and DLC-HA samples for different immersion time of 1, 24, 48, 72, 96 and 120 h in SBF solution (A scheme of the different layers for DLC-HA sample at 48 and 72 h was shown).

Table 2
EIS analysis parameters of the NiTi alloy and DLC sample for immersion time of 1, 24, 48, 72, 96, and 120 h in SBF at 37 °C.

Sample	Immersion time (h)	R_{sol} (Ω)	R_{DLC} (kΩ.cm^2)	CPE_{DLC} (μF.cm^{-2}.s^{n-1})	n_{DLC}	R_{pro} or R_{ct} (kΩ.cm^2)	CPE_{pro} or CPE_{dl} (μF.cm^{-2}.s^{n-1})	n_{pro} or n_{dl}	d (nm)	Chi-Squared
NiTi alloy	1	24	–	–	–	522.6	0.24	0.93	–	0.00113
	24	19	–	–	–	41.3	0.27	0.91	–	0.00545
DLC	1	22	6222.1	0.11	0.88	–	–	–	–	0.00128
	24	20	2872	1.05	0.96	21.5	7.89	0.77	34	0.00063
	48	20	87.3	6.02	0.83	134.2	2.458	0.82	108	0.00054
	72	18	1.2	8.35	0.83	0.11	137.6	0.84	2	0.00047
	96	16	11.4	1.68	0.94	108.3	13.4	0.78	–	0.00018
	120	16	1.3	1.59	0.97	41.5	13.3	0.79	20	0.00013

Table 3
EIS analysis parameters of DLC-HA for immersion time of 1, 24, 48, 72, 96, and 120 h in SBF at 37 °C.

Sample	Immersion time (h)	R_{sol} (Ω)	R_{HA} (kΩ.cm^2)	CPE_{HA} (μF.cm^{-2}.s^{n-1})	n_{HA}	R_{DLC} (kΩ.cm^2)	CPE_{DLC} (μF.cm^{-2}.s^{n-1})	n_{DLC}	R_{pro} or R_{ct} (kΩ.cm^2)	CPE_{pro} or CPE_{dl} (μF.cm^{-2}.s^{n-1})	n_{pro} or n_{dl}	d (nm)	Chi-Squared
DLC-HA	1	26	13.2	10.7	0.92	11230	6.24	0.91	–	–	0.91	–	0.00174
	24	25	0.2	3.55	0.75	0.9	2.28	0.81	0.1	109.8	0.91	3	0.00026
	48	24	0.3	4.50	0.74	9.1	1.33	0.84	1821	7.13	0.88	–	0.00025
	72	24	0.3	5.55	0.73	8.8	1.24	0.84	678.3	6.73	0.88	–	0.00024
	96	23	0.2	3.94	0.75	9.1	2.60	0.82	4.9	1.75	0.75	152	0.00026
	120	21	0.2	4.63	0.74	15.1	2.59	0.81	1.7	16.8	0.67	16	0.00039

presence of graphite particles in the coating (GIXRD pattern in Fig. 1a). The porous hydroxyapatite increases the friction coefficient by about 5.6 times and the large fluctuations observed from the DLC coating can be attributed to the more fragile and brittle nature and dominant abrasion wear mechanism [21,22,42]. However, the interplay between the DLC under layer and the HA top layer significantly influences the overall mechanical and tribological behavior of the HA-DLC coating. The initial smoothing effect observed upon HA deposition, where the surface roughness decreases due to pore filling, is counteracted by the inherent brittleness and porosity of the HA itself. This results in a composite structure where the HA layer, while providing bioactive properties, also introduces new wear mechanisms, such as adhesion and plastic deformation, in addition to the abrasion seen in the DLC coating alone. The reduction in hardness after HA deposition reflects the lower intrinsic hardness of HA compared to DLC, and the increased friction coefficient is likely attributable to the HA layer's increased surface area and adhesive tendencies [50,56–58]. These results highlight the complex relationship between the individual layer properties and the overall performance of the HA-DLC system, emphasizing the need for careful optimization of the HA deposition process to balance bioactivity with mechanical durability.

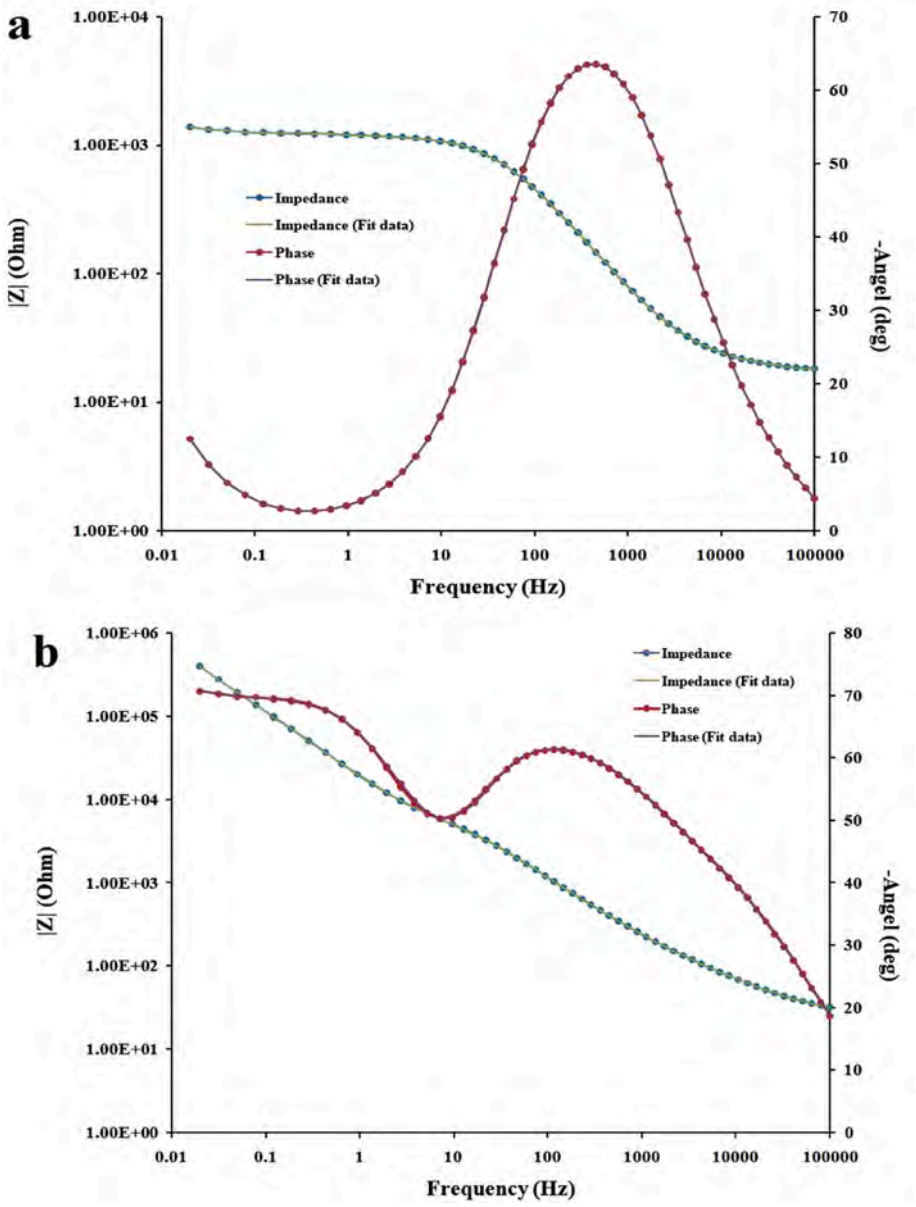

Fig. 9. Fitted curves of (a) DLC and b) DLC-HA after immersion for 72 h in SBF at 37 °C.

3.4. Relationships governing nano-mechanical properties and corrosion behavior of DLC and HA-DLC coatings

The interplay between nano-mechanical properties and corrosion resistance in DLC and HA-DLC coatings plays a vital role in their long-term performance. While the DLC layer offers exceptional hardness and wear resistance, its internal stress can influence durability in corrosive conditions. The HA top layer, though beneficial for bioactivity, introduces porosity that initially allows electrolyte penetration but later aids in protective calcium phosphate formation. Adhesion strength between layers is crucial, as a weak bond accelerates degradation [50, 56–58]. Additionally, changes in friction and wear mechanisms further shape the coating's stability, highlighting the delicate balance between mechanical integrity and corrosion protection.

The mechanical and tribological properties of the HA-DLC bilayer are significantly influenced by the DLC underlayer's characteristics. As mentioned before, the PIII&D process employing a bias voltage of −4.0 kV and an Ar/C2H2 ratio of 1:5 leads to a high sp3 carbon content. This results in a DLC layer with a hardness of approximately 13.42 GPa, as reported in the original text. This hardness is crucial for load support and wear resistance. However, the inherent compressive stress within the DLC film, while not explicitly quantified, can impact its long-term durability in corrosive environments. Studies have shown that highly stressed DLC films are more susceptible to cracking and delamination in aqueous solutions, providing pathways for electrolyte penetration to the underlying NiTi substrate [60,61]. This effect could be exacerbated at the observed operating temperatures (37 °C and 40 °C), as thermal stresses can further compromise the adhesion of the DLC to the NiTi.

The HA top layer introduces both benefits and drawbacks to the overall mechanical and corrosion performance. The sol-gel process parameters (specific precursor concentrations, pH 2) result in an HA coating with a thickness of 800 nm, as determined by XPS depth profiling. The HA's intrinsic hardness is considerably lower than that of the DLC, measuring approximately 2.1 GPa. This reduction in overall hardness is a trade-off for the HA's bioactivity. The HA's inherent porosity, resulting from the sol-gel process, presents a significant challenge to the corrosion resistance. However, this porosity also facilitates the precipitation of calcium phosphate from the SBF solution,

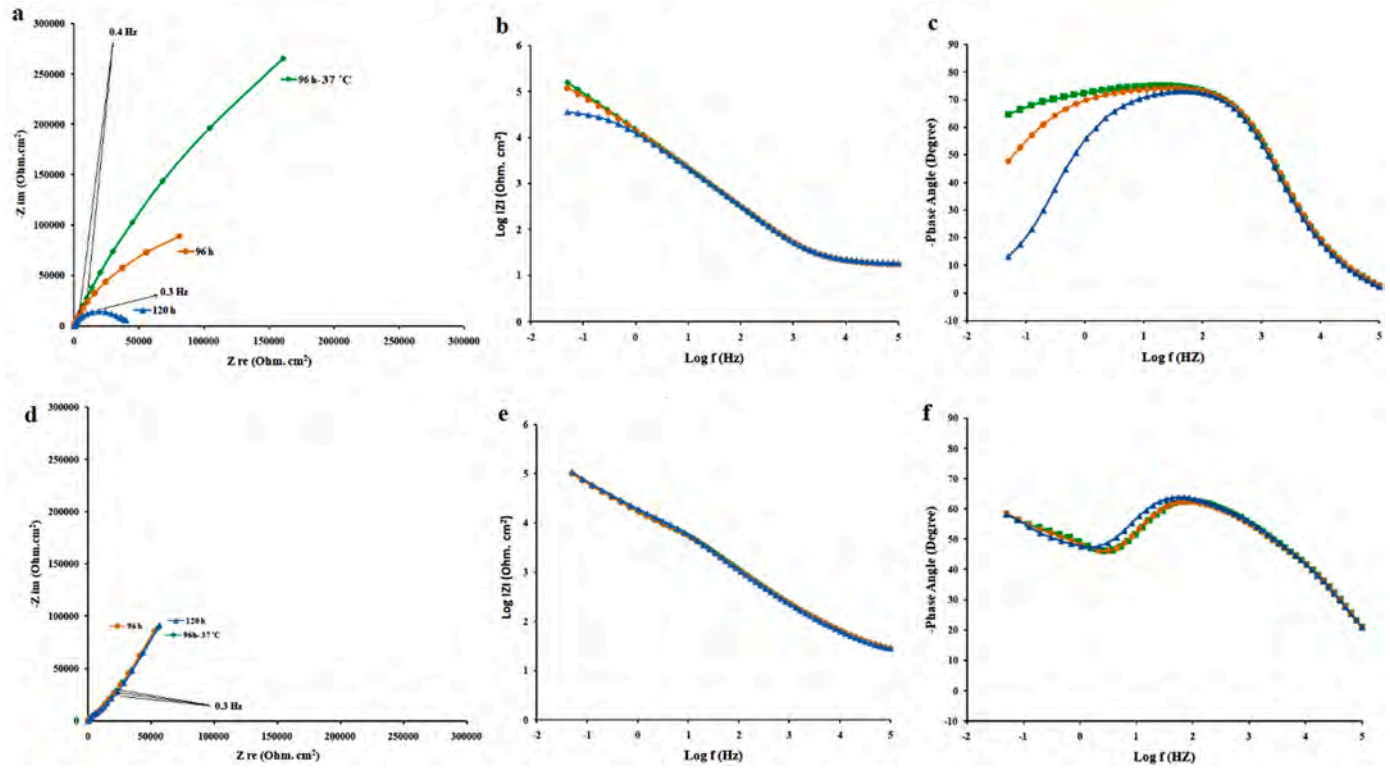

Fig. 10. Nyquist, Bode, and Bode-phase plots: (a–c) DLC and (d–f) DLC-HA after immersion for 96 h and 120 in SBF at 40 °C (plot of 96 h immersion time at 37 °C is also shown for comparison).

Table 4
EIS analysis parameters of DLC and DLC-HA after immersion for 96 and 120 h in SBF at 40 °C.

Sample	Immersion time (h)	R_{sol} (Ω)	R_{HA} (kΩ. cm^2)	CPE_{HA} (μF. $cm^{-2}.s^{n-1}$)	n_{HA}	R_{DLC} (kΩ. cm^2)	CPE_{DLC} (μF. $cm^{-2}.s^{n-1}$)	n_{DLC}	R_{pro} or R_{ct} (kΩ.cm^2)	CPE_{pro} or CPE_{dl} (μF. cm-2.s^{n-1})	n_{pro} or n_{dl}	d (nm)	Chi-Squared
DLC	96	18	0.1	1.63	0.96	255.7	14.1	0.78	–	–	–		0.00015
	120	18	0.1	1.62	0.97	39.2	14.2	0.78	–	–	–		0.00009
DLC-HA	96	22	0.2	4.08	0.75	8.8	2.88	0.82	205.3	18.4	0.71	14	0.00025
	120	21	0.2	4.3	0.82	13.6	2.85	0.82	4.1	17.1	0.82	16	0.00031

potentially leading to pore blockage and enhanced corrosion protection over time. The initial corrosion tests revealed that the HA-DLC coating exhibited an initial decrease in impedance modulus, indicating electrolyte penetration through the HA layer. However, after prolonged immersion (72 h–120 h), the impedance modulus increased, suggesting the formation of a protective calcium phosphate layer.

The interplay between the mechanical properties and corrosion behavior is further modulated by the adhesive strength between the DLC and HA layers. A strong interfacial bond is essential for preventing delamination and maintaining the coating's integrity in corrosive environments. The micro-scratch test results, indicating a critical load of 2.38 N for HA detachment, provide a measure of this adhesion strength. This adhesive strength is sufficient for biomedical applications. A weak interface would allow for easier electrolyte penetration and accelerated corrosion. Moreover, the observed increase in friction coefficient (from 0.054 for DLC to 0.304 for HA-DLC) suggests a change in the wear mechanism due to the HA layer. The higher surface roughness and adhesive tendencies of the HA layer can promote adhesion wear and plastic deformation, potentially exposing the underlying DLC and NiTi to the corrosive environment.

3.5. Antibacterial properties and biocompatibility

The bacteria image and number of *E.coli* colonies on the NiTi alloy, DLC, and DLC-HA samples after culturing for 24 h (Fig. 16), indicates 64 % decreasing in the number of *E. coli* colonies on the DLC-HA compared to DLC. In fact, the DLC coating has adverse effects on the antibacterial properties against *E.coli*. The porous hydroxyapatite coating show localized corrosion and inherent anti-bacterial properties [62], leading to a downward trend in the corrosion resistance from NiTi alloy, DLC and DLC-HA in addition to release Ni ions of 0.0038 ± 0.00014, 0.0027 ± 0.00032 and 0.0045 ± 0.00025 mg/L.cm^2 after immersion for 24 h in SBF. Fadlallah et al. [63] and Liu et al. [64] have reported that the concentration of Ni ions released by the corrosion process plays an important role in controlling the chromosome damage of the bacteria. Ni ions are capable of substituting for divalent metals (Ca, Mg, and Zn) in enzymes and proteins and changing the molecular structure. Ni release has two effects, enhancing the antibacterial properties and showing cytotoxicity [1,63–65]. Bacteria growth and adhesion depend on surface properties such as the roughness and surface energy [32,66,67] and Ni release may hinder the formation of biofilms. The SEM images of the bacteria on the NiTi alloy, DLC, and DLC-HA samples after culturing for 24 h (Fig. 17) indicate less bacteria attachment on DLC and DLC-HA.

The MTT assay is based on the direct correlation between the activity

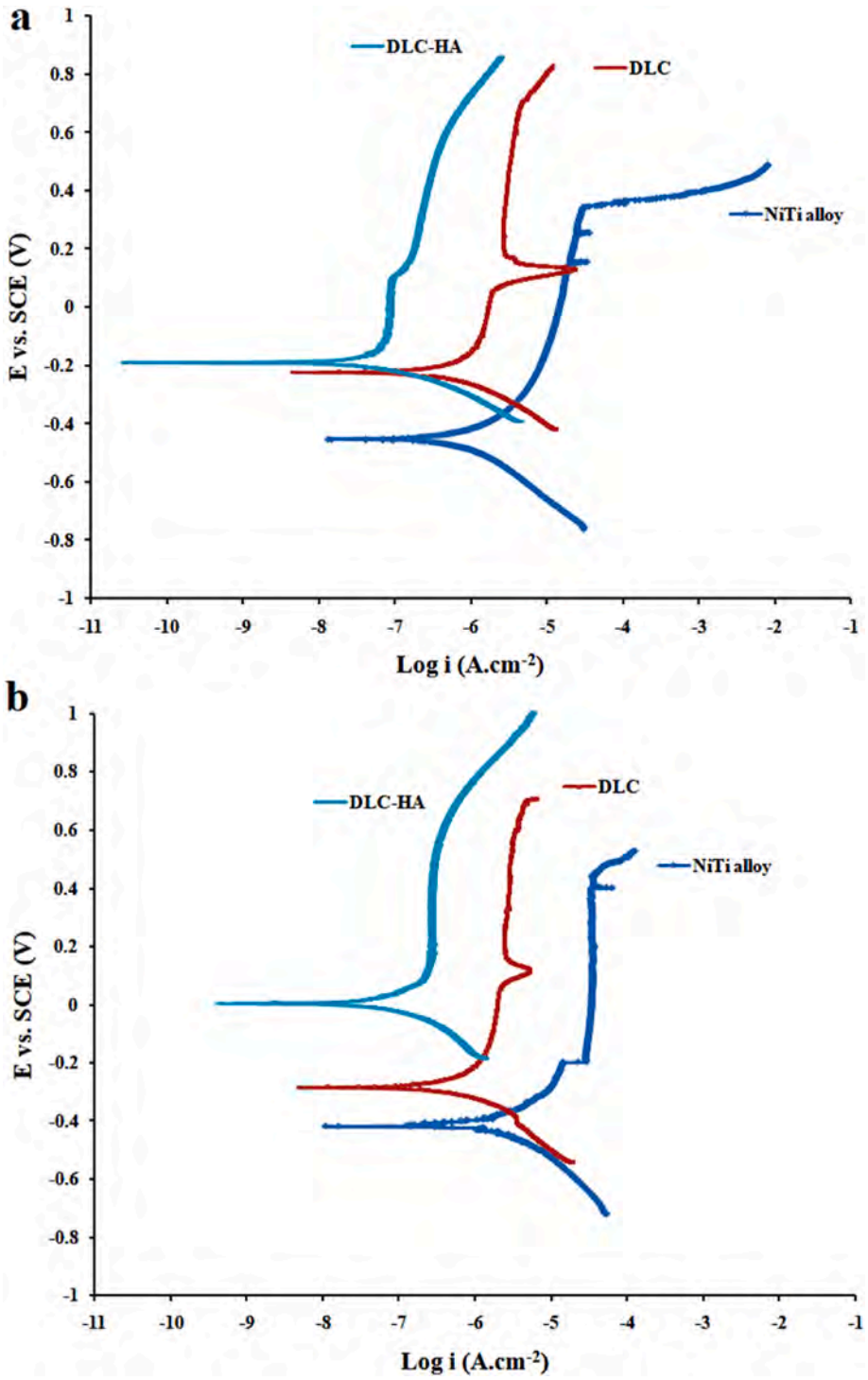

Fig. 11. Potentiodynamic curves of the NiTi alloy after 24 h and DLC and DLC-HA sample after 120 h in SBF solution at (a) 37 °C and (b) 40 °C.

Table 5
Corrosion rates and polarization parameters of the NiTi alloy after immersion for 24 h and DLC and DLC-HA after 120 h at (a) 37 °C and (b) 40 °C.

Sample	T (°C)	Immersion time (h)	E_{corr} (mV)	i_{corr} (μA/ cm^2)	$i_{passive}$ (μA/ cm^2)	β_c (mV/ decade)	β_a (mV/ decade)	Ni^{+2} (μg/cm^2)	Corrosion rate (mm/ y)
NiTi alloy	**37**	**24**	−453 ± 1	0.3 ± 0.04	–	78 ± 5	76 ± 9	240.1 ± 2.8	19296E-6
DLC		**120**	−225 ± 1	0.19 ± 0.02	1.05	63 ± 4	53 ± 6	19.3 ± 0.3	9741E-6
DLC-HA		**120**	−189 ± 1	0.04 ± 0.01	0.07	57 ± 4	41 ± 3	18.6 ± 1.2	349E-6
NiTi alloy	**40**	**24**	−417 ± 1	0.74 ± 0.04	–	78 ± 8	54 ± 7	310.7 ± 2.5	36345E-6
DLC		**120**	−295 ± 1	0.23 ± 0.03	1.46	119 ± 11	46 ± 9	71.4 ± 0.4	12375E-6
DLC-HA		**120**	3 ± 1	0.06 ± 0.02	0.21	142 ± 10	52 ± 7	12.8 ± 0.2	583E-6

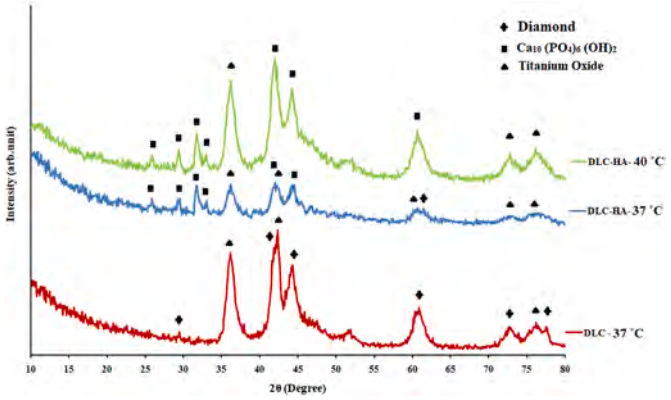

Fig. 12. GIXRD patterns of DLC and DLC-HA acquired after the polarization test and immersion in SBF for 120 h at 37 °C and 40 °Cat an incident angle of 1°.

of mitochondrial dehydrogenase of living cells and number of cells attached to the substrate [68]. It is carried out after culturing the MC3T3 cells for 1, 4, and 7 days. Fig. 18 shows that the number of cells on DLC-HA increases from the 1st to 7th day and the highest biocompatibility is observed after 7 days. Cell proliferation is an important factor to investigate the biocompatibility and cytotoxicity and our results are in line with those of Umit Erdem et al. [62]. The number of cells on the bare NiTi alloy increases from day 1–4 but decrease on the 7th day possibly due to increased corrosion and release of Ni^{+2} producing negative effects on the MC3T3 cells. All in all, DLC-HA shows enhanced corrosion resistance, biocompatibility, life time, and performance.

The 64 % reduction in E. coli adhesion on the HA-DLC surface after 24 h, as evidenced by CFU counts and SEM images (Figs. 16 and 17, is attributed to several synergistic factors. First, the nano-scale surface topography of the HA layer plays a significant role. Sol-gel derived HA coatings typically exhibit a roughened surface with features that can disrupt bacterial adhesion [69,70]. The specific parameters of our sol-gel process, including the concentrations of precursors, pH, and calcination temperature, likely yielded a surface topography that is less conducive to bacterial attachment compared to the polished NiTi or the relatively smoother DLC surface. Second, the HA surface possesses a net negative charge in physiological solutions, which can electrostatically repel negatively charged bacterial cell walls. Finally, the controlled release of nickel ions from the HA-DLC coating during the initial 24 h, while seemingly counterintuitive, appears to contribute to the observed antibacterial effect. Although HA-DLC exhibited a higher Ni leaching rate (0.0045 ± 0.00025 mg/L.cm^2) compared to NiTi and DLC-NiTi, the released Ni ions, at these concentrations, likely exerted a localized bactericidal effect without significantly compromising the overall biocompatibility [26,46,65].

The improved biocompatibility of the HA-DLC-NiTi samples, as indicated by the MTT assay (Fig. 18), is also connected to the surface properties. The sustained increase in MC3T3 cell proliferation over 7 days on the HA-DLC surface suggests that the HA layer provides a favorable environment for cell adhesion, spreading, and growth. The

Table 6
Summary of results acquired from nano-indentation tests of the NiTi alloy, DLC and DLC-HA samples.

Sample	Hardness (GPa)	Elastic Modulus (GPa)	Stiffness (μN/nm)	Max Depth (nm)	Max Force (μN)	Contact area (nm^2)	Critical load (N)
NiTi alloy	5.36 ± 0.49	86.4 ± 0.8	47.6 ± 2.8	100 ± 12	1276 ± 31	2.383E+5	–
DLC	13.42 ± 0.25	188.8 ± 2.7	135.7 ± 4.9	161 ± 18	5446 ± 18	4.058E+5	2.31 ± 0.07
DLC-HA	2.1 ± 0.14	19.6 ± 1.2	28.5 ± 2.7	230 ± 23	1652 ± 31	1.623E+6	2.38 ± 0.01

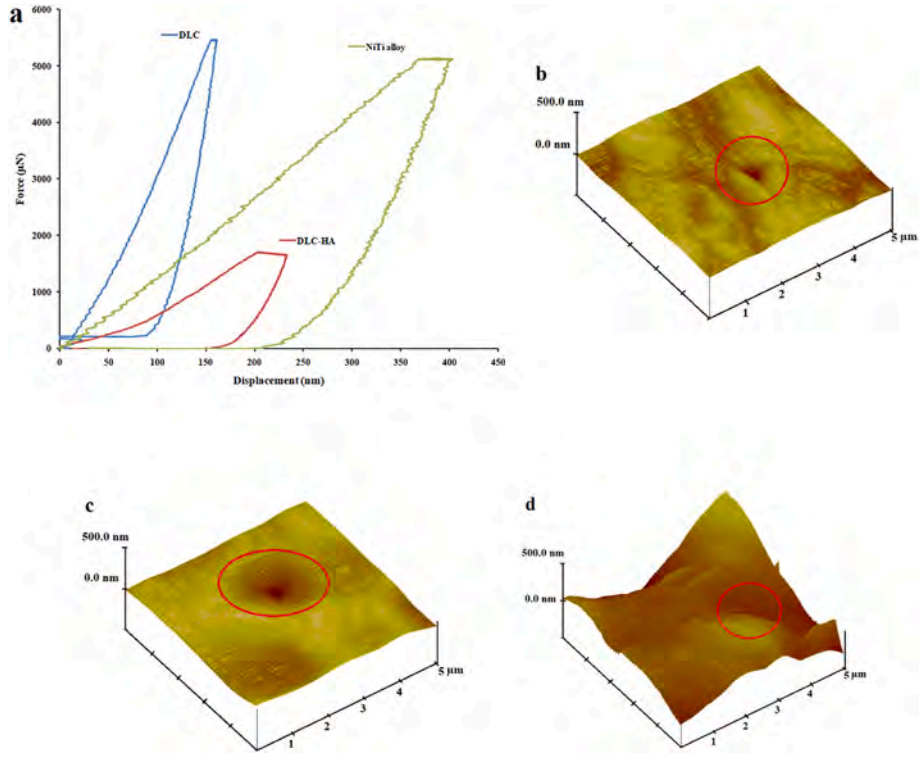

Fig. 13. (a) Nano indentation plots of the NiTi alloy, DLC and DLC-HA samples; AFM images after the nano-indentation test: (b) NiTi, (c) DLC, and (d) DLC-HA.

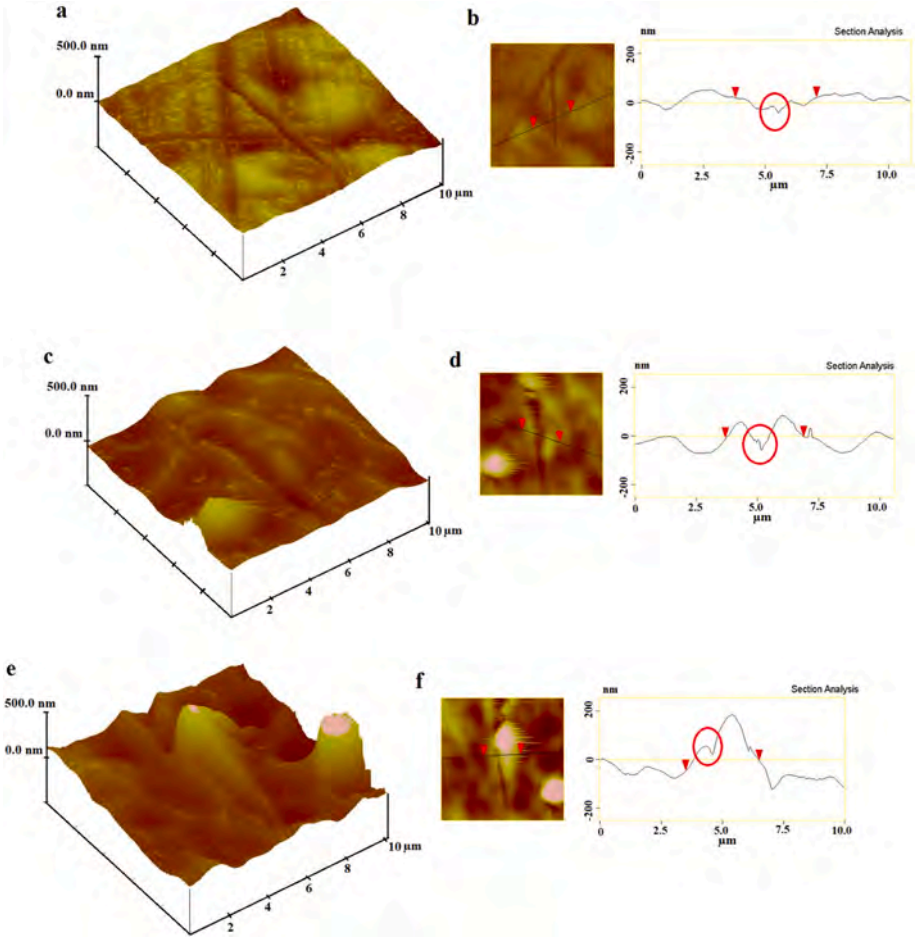

Fig. 14. AFM images and surface profiles of the scratch tracks: (a) Bare NiTi alloy, (b) DLC, and (c) DLC-HA.

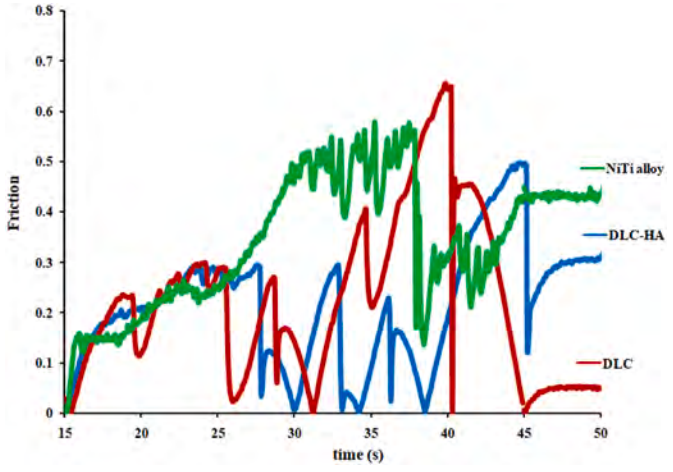

Fig. 15. Friction vs. time plots of the NiTi alloy, DLC and DLC-HA samples obtained from the scratch test.

increased surface area and the presence of calcium and phosphate ions promote osteoblast attachment and differentiation [71,72]. Furthermore, the HA layer's ability to control the Ni release rate, despite the initially higher leaching, contributes to the long-term biocompatibility. By acting as a barrier, the HA layer prevents the burst release of Ni ions that can be cytotoxic, as observed with bare NiTi samples after 7 days. This controlled release of Ni ions within a tolerable range, combined with the osteoconductive properties of HA, creates a synergistic effect that enhances cell proliferation and overall biocompatibility. In essence, the HA-DLC coating's enhanced antibacterial activity and biocompatibility are not solely attributed to the individual properties of either material but rather arise from a carefully orchestrated interplay of surface topography, surface charge, controlled ion release, and osteoconductive characteristics. Optimizing these factors through precise control over the deposition parameters is crucial for maximizing the benefits of this composite coating system.

4. Conclusion

This article successfully demonstrates the synergistic benefits of a novel HA-DLC bilayer coating on NiTi alloy achieved through a carefully controlled combination of PIII&D and sol-gel deposition techniques. The resulting 2.6 µm thick composite coating, characterized by a nano-scale surface roughness of 91 nm (Sa) and an optimized HA crystallite size of approximately 20–30 nm, exhibits a significant reduction in corrosion rate in SBF at 37 °C, evidenced by a 36 mV increase in Ecorr and a 0.15 µA/cm^2 decrease in icorr compared to single-layer DLC-NiTi. Notably, under elevated temperature conditions (40 °C), the HA-DLC coating maintains superior corrosion resistance, with a 298 mV increase in Ecorr and a 0.17 µA/cm^2 reduction in icorr, attributed to the formation of a stable calcium phosphate-rich passive film. The coating also demonstrates a 64 % reduction in E. coli adhesion after 24 h, linked to controlled Ni ion release (0.0045 ± 0.00025 mg/L.cm^2) and favorable surface topography. Furthermore, the sustained increase in MC3T3 cell viability over 7 days on HA-DLC confirms enhanced biocompatibility, exceeding that of uncoated NiTi and DLC-NiTi. These findings establish the HA-DLC bilayer as a promising advanced surface modification,

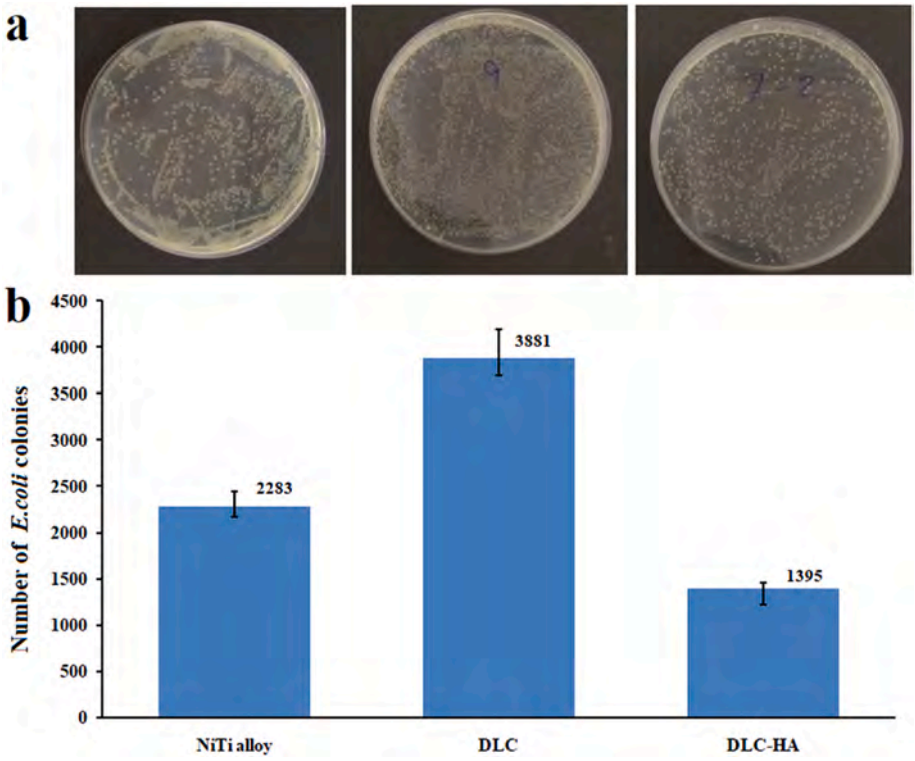

Fig. 16. Images and CFU numbers of viable *E. coli* colonies on the NiTi alloy, DLC, and DLC-HA samples at 24 h.

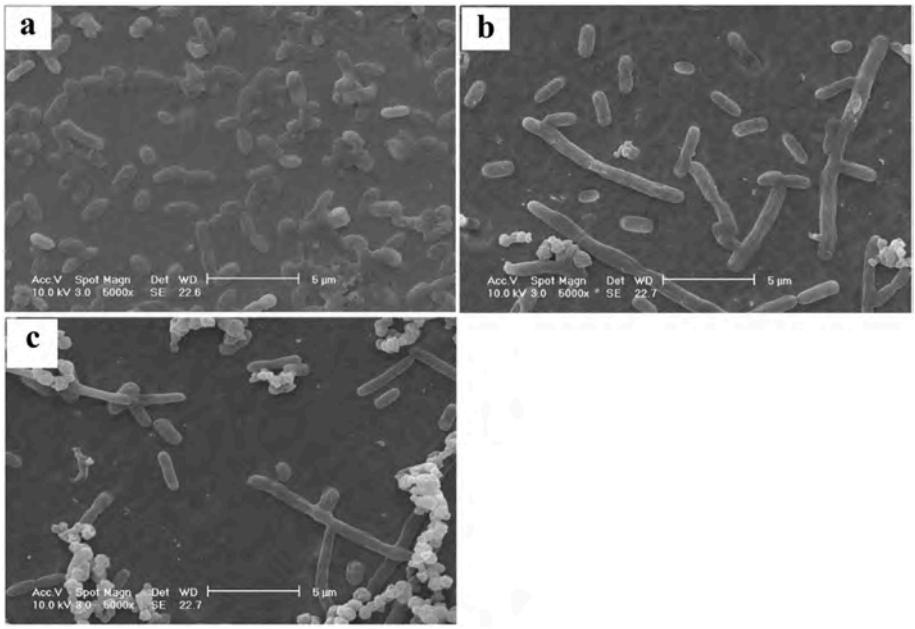

Fig. 17. SEM images of *E. coli*: (a) NiTi alloy, (b) DLC, and (c) DLC-HA after culturing 24 h.

offering a balanced combination of corrosion protection, antibacterial activity, and biocompatibility, paving the way for improved clinical outcomes and extended lifespan of NiTi biomedical implants. The design rules established from the HA-DLC composite coating are valuable for all advanced implant designs and will change the landscape of future advanced implant surface designs.

CRediT authorship contribution statement

Ali Shanaghi: Writing – original draft, Supervision, Investigation, Conceptualization. **Babak Mehrjou:** Writing – original draft, Investigation. **Armin Moradjoui Hamedani:** Formal analysis. **Ali Reza Souri:** Formal analysis. **Abdul Mateen Qasim:** Investigation. **Paul K. Chu:** Writing – review & editing, Supervision, Investigation, Conceptualization.

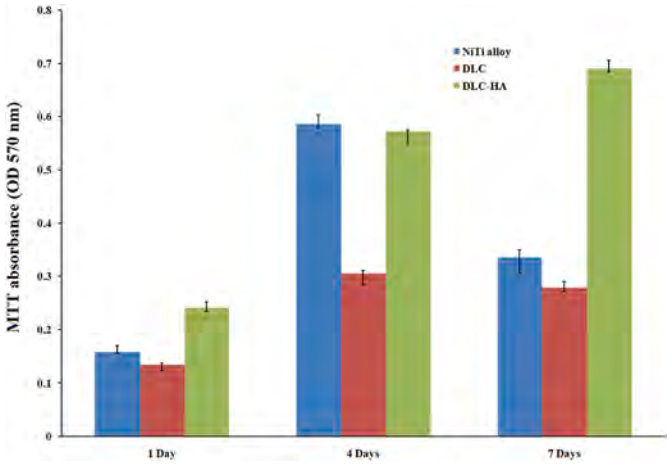

Fig. 18. MTT assay results for incubation of MC3T3 cells on the surface of NiTi alloy, DLC and DLC-HA samples, after 1, 4 and 7 days.

Declaration of competing interest

The authors declare that they have NO affiliations with or involvement in any organization or entity with any financial interest, or personal relationships that could have appeared to influence the work reported in this paper.

Acknowledgements

The work was financially supported by the Malayer University Research Grant, the City University of Hong Kong Donation Research Grant (DON-RMG 9229021), the City University of Hong Kong Donation Grant (9220061), as well as the City University of Hong Kong Strategic Research Grant (SRG) (7005505).

References

[1] S. Ao, K. Li, W. Liu, X. Qin, T. Wang, Y. Dai, Z. Luo, Electrochemical micromachining of NiTi shape memory alloy with ethylene glycol–NaCl electrolyte containing ethanol, J. Manuf. Process. 53 (2020) 223–228, https://doi.org/10.1016/j.jmapro.2020.02.019.

[2] A. Shanaghi, P.K. Chu, Enhancement of mechanical properties and corrosion resistance of NiTi alloy by carbon plasma immersion ion implantation, Surf. Coatings Technol. 365 (2019) 52–57, https://doi.org/10.1016/j.surfcoat.2018.04.027.

[3] V. Chudinov, I. Kondyurina, V. Terpugov, A. Kondyurin, Weakened foreign body response to medical polyureaurethane treated by plasma immersion ion implantation, Nucl. Instruments Methods Phys. Res. Sect. B Beam Interact. with Mater. Atoms 440 (2019) 163–174, https://doi.org/10.1016/j.nimb.2018.12.026.

[4] M. Zhu, F. Song, F. Li, X. Jin, X. Wang, L. Wang, Surface insulating properties of titanium implanted alumina ceramics by plasma immersion ion implantation, Nucl. Instruments Methods Phys. Res. Sect. B Beam Interact. with Mater. Atoms 407 (2017) 155–159, https://doi.org/10.1016/j.nimb.2017.06.005.

[5] C. Silva, M. Ueda, C.B. Mello, Metal cylindrical sieve (MCS) for plasma confinement and low sputtering nitrogen plasma immersion ion implantation, Appl. Surf. Sci. 509 (2020) 145232, https://doi.org/10.1016/j.apsusc.2019.145232.

[6] M.H. Fathi, A. Doost Mohammadi, Preparation and characterization of sol-gel bioactive glass coating for improvement of biocompatibility of human body implant, Mater. Sci. Eng. A. 474 (2008) 128–133, https://doi.org/10.1016/j.msea.2007.05.041.

[7] R. Palanivelu, S. Kalainathan, A. Ruban Kumar, Characterization studies on plasma sprayed (AT/HA) bi-layered nano ceramics coating on biomedical commercially pure titanium dental implant, Ceram. Int. 40 (2014) 7745–7751, https://doi.org/10.1016/j.ceramint.2013.12.116.

[8] M. Mozetič, Surface modification to improve properties of materials, Materials 12 (3) (2019) 441, https://doi.org/10.3390/ma12030441.

[9] M.S. Safavi, J. Khalil-Allafi, I. Ahadzadeh, F.C. Walsh, L. Visai, Improved corrosion protection of a NiTi implant by an electrodeposited HAp-Nb2O5 composite layer, Surf. Coat. Technol. 470 (2023) 129822, https://doi.org/10.1016/j.surfcoat.2023.129822.

[10] M.S. Safavi, J. Khalil-Allafi, A. Motallebzadeh, C. Volpini, V. Khalilid, L. Visai, Encouraging tribomechanical and biological responses of hydroxyapatite coatings reinforced by various levels of niobium pentoxide particles, Mater. Adv. 4 (2023) 5618–5632, https://doi.org/10.1039/D3MA00704A.

[11] Y. Zhou, M. Li, Y. Cheng, Y.F. Zheng, T.F. Xi, S.C. Wei, Tantalum coated NiTi alloy by PIIID for biomedical application, Surf. Coat. Technol. 228 (2013) S2–S6, https://doi.org/10.1016/j.surfcoat.2012.11.002.

[12] M.S. Safavi, J. Khalil-Allafi, L. Visai, Improved osteogenic activity of NiTi orthopedic implant by HAp-Nb2O5 composite coatings: materials and biological points of view, bio, Advances 150 (2023) 213435, https://doi.org/10.1016/j.bioadv.2023.213435.

[13] F. Liu, J.L. Xu, D.Z. Yu, F.P. Wang, L.C. Zhao, Wear resistance of micro-arc oxidation coatings on biomedical NiTi alloy, J. Alloys Compd. 487 (1–2) (2009) 391–394, https://doi.org/10.1016/j.jallcom.2009.07.145.

[14] W.Y. Ching, P. Rulis, A. Misra, Ab initio elastic properties and tensile strength of crystalline hydroxyapatite, Acta Biomater. 5 (2009) 3067–3075, https://doi.org/10.1016/j.actbio.2009.04.030.

[15] D. Sidane, D. Chicot, S. Yala, S. Ziani, H. Khireddine, A. Iost, X. Decoopman, Study of the mechanical behavior and corrosion resistance of hydroxyapatite sol-gel thin coatings on 316 L stainless steel pre-coated with titania film, Thin Solid Films 593 (2015) 71–80, https://doi.org/10.1016/j.tsf.2015.09.037.

[16] J.H. Sui, W. Cai, Formation of diamond-like carbon (DLC) film on the NiTi alloys via plasma immersion ion implantation and deposition (PIIID) for improving corrosion resistance, Appl. Surf. Sci. 253 (2006) 2050–2055, https://doi.org/10.1016/j.apsusc.2006.03.086.

[17] T.E. Fletcher, C.P. Bleeker-Rovers, N.J. Beeching, Fever, Med. (United Kingdom). 45 (2017) 177–183, https://doi.org/10.1016/j.mpmed.2016.12.013.

[18] V. Konovalova, The effect of temperature on the corrosion rate of iron-carbon alloys, Mater. Today Proc. 38 (2021) 1326–1329, https://doi.org/10.1016/j.matpr.2020.08.094.

[19] L. Zhang, D. Ren, H. Ji, A. Ma, E.F. Daniel, S. Li, W. Jin, Y. Zheng, Study on the corrosion behavior of NiTi shape memory alloys fabricated by electron beam melting, npj Mater. Degrad. 6 (2022) 1–8, https://doi.org/10.1038/s41529-022-00289-3.

[20] R.A. Ahmed, S.A. Fadl-Allah, N. El-Bagoury, S.M.F.G. El-Rab, Improvement of corrosion resistance and antibacterial effect of NiTi orthopedic materials by chitosan and gold nanoparticles, Appl. Surf. Sci. 292 (2014) 390–399, https://doi.org/10.1016/j.apsusc.2013.11.150.

[21] J. Ryhänen, E. Niemi, W. Serlo, E. Niemelä, P. Sandvik, H. Pernu, T. Salo, Biocompatibility of nickel-titanium shape memory metal and its corrosion behavior in human cell cultures, J. Biomed. Mater. Res. 35 (1997) 451–457, https://doi.org/10.1002/(SICI)1097-4636(19970615)35:4<451::AID-JBM5>3.3.CO;2-X.

[22] E. Espinar-Escalona, J.M. Llamas-Carreras, J.M. Barrera-Mora, C. Abalos-Lasbrucci, F.J. Gil-Mur, Effect of temperature on the orthodontic clinical applications of NiTi closed-coil springs, Med. Oral Patol. Oral Cir. Bucal 18 (2013), https://doi.org/10.4317/medoral.19073.

[23] N. Figueira, T.M. Silva, M.J. Carmezim, J.C.S. Fernandes, Corrosion behaviour of NiTi alloy, Electrochim. Acta 54 (2009) 921–926, https://doi.org/10.1016/j.electacta.2008.08.001.

[24] D.K. Pun, D.W. Berzins, Corrosion behavior of shape memory, superelastic, and nonsuperelastic nickel-titanium-based orthodontic wires at various temperatures, Dent. Mater. 24 (2008) 221–227, https://doi.org/10.1016/j.dental.2007.05.003.

[25] A.M. Qasim, F. Ali, H. Wu, R.K.Y. Fu, S. Xiao, Y. Li, Z. Wu, P.K. Chu, Enhanced mechanical and electrochemical properties of TiNx thin films prepared by magnetron sputtering with an anode layer ion source, Surf. Coat. Technol. 365 (2019) 253–260, https://doi.org/10.1016/j.surfcoat.2018.07.076.

[26] A. Shanaghi, B. Mehrjou, Z. Ahmadian, A.R. Souri, P.K. Chu, Enhanced corrosion resistance, antibacterial properties, and biocompatibility by hierarchical hydroxyapatite/ciprofloxacin-calcium phosphate coating on nitrided NiTi alloy, Mate. Sci. Eng. C. 118 (2021) 111524, https://doi.org/10.1016/j.msec.2020.111524.

[27] M. Kazemi, S. Ahangarani, M. Esmailian, A. Shanaghi, Investigation on the corrosion behavior and biocompatibility of Ti-6Al-4V implant coated with HA/TiN dual layer for medical applications, Surf. Coat. Technol. 397 (2020) 126044, https://doi.org/10.1016/j.surfcoat.2020.126044.

[28] T. Kokubo, H. Takadama, How useful is SBF in predicting in vivo bone bioactivity? Biomaterials 27 (2006) 2907–2915, https://doi.org/10.1016/j.biomaterials.2006.01.017.

[29] M. Kazemi, S. Ahangarani, M. Esmailian, A. Shanaghi, Investigating the corrosion performance of Ti-6Al-4V biomaterial alloy with hydroxyapatite coating by artificial neural network, Mate. Sci. Eng. B. 278 (2022) 115644, https://doi.org/10.1016/j.mseb.2022.115644.

[30] M. Rabiei, A. Palevicius, A. Monshi, S. Nasiri, A. Vilkauskas, G. Janusas, Comparing methods for calculating nano crystal size of natural hydroxyapatite using X-Ray diffraction, Nanomaterials 10 (9) (2020) 1627, https://doi.org/10.3390/nano10091627.

[31] A. Shanaghi, A.R. Souri, M. Rafie, P.K. Chu, Nano-mechanical properties of zirconia-alumina-benzotriazole nano-composite coating deposited on Al2024 by the sol-gel method, Thin Solid Films 689 (2019) 137417, https://doi.org/10.1016/j.tsf.2019.137417.

[32] T.S. Li, H. Li, F. Pan, Microstructure and nanoindentation hardness of Ti/TiN multilayered films, Surf. Coat. Technol. 137 (2001) 225–229, https://doi.org/10.1016/S0257-8972(00)01096-3.

[33] W.C. Oliver, G.M. Pharr, An improved technique for determining hardness and elastic modulus using load and displacement sensing indentation experiments, J. Mater. Res. 7 (1992) 1564–1583.

[34] R.J. Narayan, Hydroxyapatite-diamondlike carbon nanocomposite films, Mater. Sci. Eng. C. 25 (2005) 398–404, https://doi.org/10.1016/j.msec.2005.01.023.
[35] J. Qi, F. Xu, K. Bao, P. Li, D. He, K. Chen, Q. Wang, Influence of a hard transition layer on the microstructure and properties of diamond-like carbon/hydroxyapatite composite coating prepared by magnetron sputtering, J. Eur. Ceram. Soc. 41 (2021) 3731–3742, https://doi.org/10.1016/j.jeurceramsoc.2021.01.006.
[36] X.J. Ji, L. Gao, J.C. Liu, R.Z. Jiang, F.Y. Sun, L.Y. Cui, S.Q. Li, K.Q. Zhi, R.C. Zeng, Z.L. Wang, Corrosion resistance and antibacterial activity of hydroxyapatite coating induced by ciprofloxacin-loaded polymeric multilayers on magnesium alloy, Prog. Org. Coatings. 135 (2019) 465–474, https://doi.org/10.1016/j.porgcoat.2019.06.048.
[37] K. McLeod, S. Kumar, R.S.C. Smart, N. Dutta, N.H. Voelcker, G.I. Anderson, R. Sekel, XPS and bioactivity study of the bisphosphonate pamidronate adsorbed onto plasma sprayed hydroxyapatite coatings, Appl. Surf. Sci. 253 (2006) 2644–2651, https://doi.org/10.1016/j.apsusc.2006.05.031.
[38] P.M. Dietrich, A. Hennig, M. Holzweber, T. Thiele, H. Borcherding, A. Lippitz, U. Schedler, U. Resch-Genger, W.E.S. Unger, Surface analytical study of poly (acrylic acid)-grafted microparticles (beads): characterization, chemical derivatization, and quantification of surface carboxyl groups, J. Phys. Chem. C 118 (2014) 20393–20404, https://doi.org/10.1021/jp505519g.
[39] N. Paik, Raman and XPS studies of DLC films prepared by a magnetron sputter-type negative ion source, Surf. Coat. Technol. 200 (2005) 2170–2174, https://doi.org/10.1016/j.surfcoat.2004.08.073.
[40] E.C. Samano, G. Soto, A. Olivas, L. Cota, DLC thin films characterized by AES, XPS and EELS, Appl. Surf. Sci. 202 (2002) 1–7, https://doi.org/10.1016/S0169-4332(02)00891-7.
[41] P. Mérel, M. Tabbal, M. Chaker, S. Moisa, J. Margot, Direct evaluation of the sp 3 content in diamond-like-carbon films by XPS, Appl. Surf. Sci. 136 (1998) 105–110, https://doi.org/10.1016/S0169-4332(98)00319-5.
[42] H. Cicek, Wear behaviors of TiN/TiCN/DLC composite coatings in different environments, Ceram. Int. 44 (2018) 4853–4858, https://doi.org/10.1016/j.Ceram.Int.2017.12.074.
[43] S.A.X. Stango, D. Karthick, S. Swaroop, U.K. Mudali, U. Vijayalakshmi, Development of hydroxyapatite coatings on laser textured 316 LSS and Ti-6Al-4V and its electrochemical behavior in SBF solution for orthopedic applications, Ceram. Int. 44 (2018) 3149–3160, https://doi.org/10.1016/j.ceramint.2017.11.083.
[44] B. Hirschorn, M.E. Orazem, B. Tribollet, V. Vivier, I. Frateur, M. Musiani, Determination of effective capacitance and film thickness from constant-phase-element parameters, Electrochim. Acta 55 (2010) 6218–6227, https://doi.org/10.1016/j.electacta.2009.10.065.
[45] C. Sun, J. Li, S. Shuang, H. Zeng, J.L. Luo, Effect of defect on corrosion behavior of electroless Ni-P coating in CO2-saturated NaCl solution, Corros. Sci. 134 (2018) 23–37, https://doi.org/10.1016/j.corsci.2018.01.041.
[46] M. Chembath, J.N. Balaraju, M. Sujata, In vitro corrosion studies of surface modified NiTi alloy for biomedical applications, Adv. Biomater. 2014 (2014) 1–13, https://doi.org/10.1155/2014/697491.
[47] T. Hu, C. Chu, Y. Xin, S. Wu, K.W.K. Yeung, P.K. Chu, Corrosion products and mechanism on NiTi shape memory alloy in physiological environment, J. Mater. Res. 25 (2010) 350–358, https://doi.org/10.1557/jmr.2010.0051.
[48] N. Eliaz, Corrosion of metallic biomaterials: a review, Materials 12 (2019), https://doi.org/10.3390/ma12030407.
[49] I.B. Camargo, J.E. Van Sickels, Surgical complications after implant placement, Dent. Clin. North Am. 59 (2015) 57–72, https://doi.org/10.1016/j.cden.2014.08.003.
[50] P.N. Chavan, M.M. Bahir, R.U. Mene, M.P. Mahabole, R.S. Khairnar, Study of nanobiomaterial hydroxyapatite in simulated body fluid: formation and growth of apatite, Mater. Sci. Eng. B Solid-State Mater. Adv. Technol. 168 (2010) 224–230, https://doi.org/10.1016/j.mseb.2009.11.012.
[51] B. Díaz, E. Härkönen, J. Światowska, V. Maurice, A. Seyeux, P. Marcus, M. Ritala, Low-temperature atomic layer deposition of Al2O3 thin coatings for corrosion protection of steel: surface and electrochemical analysis, Corros. Sci. 53 (2011) 2168–2175, https://doi.org/10.1016/j.corsci.2011.02.036.
[52] A. Shanaghi, M. Kadkhodaie, Investigation of high concentration of benzotriazole on corrosion behaviour of titania–benzotriazole hybrid nanostructured coating applied on Al 7075 by the sol–gel method, Corros. Eng. Sci. Technol. 52 (2017) 332–342, https://doi.org/10.1080/1478422X.2017.1288353.
[53] R.C. Hibbeler, Mechanics of Materials, tenth ed., Pearson, 2016. ISBN-13: 9780134319650.
[54] R. Xiang, J. Huang, X. Yu, H. Zhao, X. Song, D. Fan, The effect of Ni/Ti atomic ratios on residual stress and deformation in WAAM of dissimilar filler wire NiTi alloys, J. Mater. Res. Technol. 35 (2025) 1813–1828, https://doi.org/10.1016/j.jmrt.2025.01.168.
[55] A. Laderou, M. Mohammadpour, S. Theodossiades, R. Daubney, G. Meeks, On the effect of DLC and WCC coatings on the efficiency of manual transmission gear pairs, Appl. Sci. 10 (9) (2020) 3102, https://doi.org/10.3390/app10093102.
[56] V.M. Suntharavel Muthaiah, M. Rajput, A. Tripathi, S. Suwas, K. Chatterjee, Electrophoretic deposition of nanocrystalline calcium phosphate coating for augmenting bioactivity of additively manufactured Ti-6Al-4V, ACS materials Au 2 (2) (2021) 132–142, https://doi.org/10.1021/acsmaterialsau.1c00043.
[57] S. Ghasemi, A. Shanaghi, P.K. Chu, Nano mechanical and wear properties of multi-layer Ti/TiN coatings deposited on Al 7075 by high-vacuum magnetron sputtering, Thin Solid Films 638 (2017) 96–104, https://doi.org/10.1016/j.tsf.2017.07.049.
[58] A. Shanaghi, A.R.S. Rouhaghdam, S. Ahangarani, P.K. Chu, Effect of plasma CVD operating temperature on nanomechanical properties of TiC nanostructured coating investigated by atomic force microscopy, Mater. Res. Bull. 47 (2012) 2200–2205, https://doi.org/10.1016/j.materresbull.2012.06.003.
[59] M.D. Bentzon, C. Barholm-Hansen, J.B. Hansen, Interfacial shear strength of diamond-like carbon coatings deposited on metals, Diam. Relat. Mater. 4 (1995) 787–790, https://doi.org/10.1016/0925-9635(94)05227-1.
[60] L. Cao, J. Liu, Y. Wan, J. Pu, Corrosion and tribocorrosion behavior of W doped DLC coating in artificial seawater, Diam. Relat. Mater. 109 (2020) 108019, https://doi.org/10.1016/j.diamond.2020.108019.
[61] Z. Liu, P. Yin, C. Mou, S. Wang, L. Shang, X. Cao, G. Zhang, Q. Xue, Unraveling the corrosion behavior and mechanism of DLC film on the inner surface of N80 lengthy pipeline in CO2-H2S-Cl− environment, Surf. Coat. Technol. 494 (2024) 131350, https://doi.org/10.1016/j.surfcoat.2024.131350.
[62] U. Erdem, M. Dogan, A.U. Metin, S. Baglar, M.B. Turkoz, M. Turk, S. Nezir, Hydroxyapatite-based nanoparticles as a coating material for the dentine surface: an antibacterial and toxicological effect, Ceram. Int. 46 (2020) 270–280, https://doi.org/10.1016/j.ceramint.2019.08.260.
[63] S.A. Fadlallah, N. El-Bagoury, S.M.F. Gad El-Rab, R.A. Ahmed, G. El-Ousamii, An overview of NiTi shape memory alloy: corrosion resistance and antibacterial inhibition for dental application, J. Alloys Compd. 583 (2014) 455–464, https://doi.org/10.1016/j.jallcom.2013.08.029.
[64] J.X. Liu, D.Z. Yang, F. Shi, Y.J. Cai, Sol-gel deposited TiO2 film on NiTi surgical alloy for biocompatibility improvement, Thin Solid Films 429 (2003) 225–230, https://doi.org/10.1016/S0040-6090(03)00146-9.
[65] N. Ohtsu, S. Suginishi, M. Hirano, Antibacterial effect of nickel-titanium alloy owing to nickel ion release, Appl. Surf. Sci. 405 (2017) 215–219, https://doi.org/10.1016/j.apsusc.2017.02.037.
[66] V.T.H. Pham, V.K. Truong, A. Orlowska, S. Ghanaati, M. Barbeck, P. Booms, A. J. Fulcher, C.M. Bhadra, R. Buividas, V. Baulin, C. James Kirkpatrick, P. Doran, D. E. Mainwaring, S. Juodkazis, R.J. Crawford, E.P. Ivanova, Race for the surface: eukaryotic cells can win, ACS Appl. Mater. Interfaces 8 (2016) 22025–22031, https://doi.org/10.1021/acsami.6b06415.
[67] H.H. Tuson, D.B. Weibel, Bacteria-surface interactions, Soft Matter 9 (2013) 4368–4380, https://doi.org/10.1039/c3sm27705d.
[68] K. Suchanek, M. Perzanowski, K. Suchy, M. Lekka, B. Szaraniec, M. Marszałek, Assessment of phase stability and in vitro biological properties of hydroxyapatite coatings composed of hexagonal rods, Surf. Coatings Technol. 364 (2019) 298–305, https://doi.org/10.1016/j.surfcoat.2019.02.088.
[69] I. Georgakopoulos-Soares, E.L. Papazoglou, P. Karmiris-Obratański, N.E. Karkalos, A.P. Markopoulos, Surface antibacterial properties enhanced through engineered textures and surface roughness: a review, Colloids Surf. B Biointerfaces 231 (2023) 113584, https://doi.org/10.1016/j.colsurfb.2023.113584.
[70] K.V. Nadaraia, D.V. Mashtalyar, M.A. Piatkova, A.I. Pleshkova, I.M. Imshinetskiy, M.S. Gerasimenko, E.A. Belov, V.V. Kumeiko, D.N. Kozyrev, K.A. Fomenko, V. V. Mostovaya, B.R. Torpanov, A.R. Biktimirov, I.S. Osmushko, S.L. Sinebryukhov, S.V. Gnedenkov, Antibacterial HA-coatings on bioresorbable Mg alloy, J. Magnes. Alloy. 12 (5) (2024) 1965–1985, https://doi.org/10.1016/j.jma.2024.05.006.
[71] B. Pourmollaabbassi, S. Karbasi, B. Hashemibeni, Evaluate the growth and adhesion of osteoblast cells on nanocomposite scaffold of hydroxyapatite/titania coated with poly hydroxybutyrate, Adv. Biomed. Res. 5 (2016) 156, https://doi.org/10.4103/2277-9175.188486.
[72] M. Kobayashi, S. Nihonmatsu, T. Okawara, Adhesion and proliferation of osteoblastic cells on hydroxyapatite-dispersed Ti-based composite plate, In Vivo 33 (4) (2019) 1067–1079, https://doi.org/10.21873/invivo.11575.